Chair of Applied Geophysics

Master's Thesis

YOUNG'S ELASTIC MODULUS: COMPARING THE DYNAMIC AND STATIC APPROACHES USING STANDARD AND DEFECT-MODEL CORRELATION METHODS

Obinna Christian Muozube

January 2019

ABSTRACT

This thesis presents the correlation results of static and dynamic Young's moduli based on standard and simplified defect-model approaches for some rock intervals at two different locations. Elastic properties of rocks can be determined in two ways; either by in-situ seismic velocity measurements accomplished by logging in a borehole, or by compressive tests carried out on sample cores drawn from such borehole. The first method defines the dynamic Young's modulus determination. And the later defines the static method. However, these two measurement methods do not give the same results or values. Studies have shown that the difference in values stems from their differential strain amplitude. While the strain amplitude of static Young's moduli is in the order of 10^{-3} to 10^{-2}, that of the dynamic Young's moduli is much smaller and in the order of 10^{-7} to 10^{-6}. Therefore, conventional practices has been applied over time in finding correlations between the two, so that whenever one with easier and cheaper means of measurement is estimated, the other could be derived based on the established correlations. Recently, the focus shifted to removing or correcting for factors that brings about disparity in measured values of the two properties. So that a singular measurement using either of the methods could approximate or equal the other. One of such correction is the application of the simplified defect model. This model tend to compensate or rather improve the in-situ static (Young's modulus) estimates with respect to the contributions of defects such as fractures, microcracks and intergranular boundaries. These defects tend to close up in laboratory measurements giving higher laboratory values that yields lower in-situ static estimates. Hence, this thesis not only compares measured values of the two elastic properties and their standard correlations, but also discusses the application of the aforementioned model on available log data.

The measurements were already taken by the research institutions and data made available for analysis in this work. However, standard measurement procedures were discussed, for more insightful and objective appraisal of the data quality. Velocity values from full wave sonic (FWS) logs were used to calculate the in-situ dynamic Young's moduli, otherwise referred to as the dynamic log data. And velocity values recorded for the ultrasonic laboratory measurements were similarly used to calculate the dynamic Young's moduli in the laboratory (dynamic lab data).

The velocity measurements for the first location (location 1) were carried out simultaneously with its uniaxial compressive tests, while those of the second location (location 2), being a product of much older research, were isolated measurements. Static Young's moduli on the other hand were determined through uniaxial compressive tests. The process involves the compression of adequately sized core samples by gradually increasing the stress applied longitudinally to them; and then recording the lengthwise increase or decrease in deformations (strains) for corresponding stress increments. It is common practice to apply stress till the core fractures or totally crumbles, and then the stress at this point recorded as the ultimate stress or the so-called uniaxial compressive strength (UCS). This was the case for data from location 2; but the data made available for location 1 indicated that stress was applied up to a certain maximum (approximately 60 MPa) in each core measurement, and then gradually withdrawn. The so-called loading and unloading sessions. However, static moduli calculations were based on the loading sessions only. The calculation was carried out by adopting the tangent-modulus method. This method involves a plot of the stress-strain values, follwed by establishment of a tangent to the resulting stress-strain curve at a point corresponding to 50% of the maximum (ultimate) stress before unloading or fracture, and lastly determination of the slope of the tangent. The slope becomes the static Young's modulus for the core so tested. Two major rock types, granite-gneiss and white schist were traversed by borehole 10 at location 1. The log data provided for borehole 8 in the same location indicated gradation of sort from granite-gneiss to diorite-hornblende-gneiss in the deeper section, while borehole 9 is composed entirely of granite-gneiss. There was no static data for borehole 8, while borehole 9 has no log data. At location 2, the pilot borehole traversed a lengthy section of gneiss with varying blends of other rock types which were distinguishable at certain depth intervals. At the deepest section of the borehole, were predominantly granite-amphibolite. Standard correlation of the calculated dynamic and static values for all the rock types was by linear regression plots of just the laboratory measured properties. Correlation for the composite gneiss section in the pilot borehole were first carried out for individual units (Gneiss, Hornblende-gneiss and Biotite-gneiss), and then as a combined unit of all the gneiss intervals. The decision was made to use the combined unit for subsequent analysis as there were no meaningful advantage in using the individual gneiss intervals.

On the other hand, it was assumed that using the combined unit has the comparative advantage of giving a wholesome coverage of the borehole section with possible unified data, and would guarantee a continous elastic property assessment.

To apply the simplified defect model concept, first a model was computed for the dynamic property. This dynamic model represents an equivalent to the in-situ dynamic (log) data. That is, what the dynamic lab data should be, had it not been affected by the closure of defects. Furthermore, the dynamic model was computed based on the obvious relationship between the dynamic lab data and the square of velocities measured in the laboratory. Also, from the dynamic model, a corresponding static model was computed based on the widely conceived relationship between static and dynamic properties. As a result, the established relationship between the model dynamic and model static data became the defect correlation model. This model (equation) as generated for each rock type or group was then applied to corresponding dynamic log data and analysed in log sections. Model results were considered successful if they not only improve the correlation result achieved with the standard method, but most importantly show good match with the dynamic log data as well as the measured core data.

The standard correlation method gave good results for the granite-gneiss and white schist rock types of location 1. Regression coefficients of 0.82 and 0.999 respectively were recorded for their correlations. Location 2 on the other hand, produced poor results. Regression coefficient for the standard correlation of the combined gneiss intervals was particularly very poor (0.01); while that of the granite-amphibolite was relatively higher (0.30) but not good enough. Application of the defect-model proved succesful for the granite-gneiss and the combined gneiss intervals. However, while the model result for the granite-gneiss showed improvement in its regression coefficient from the earlier 0.82 to 0.91 with a very good match for the measured core data and dynamic log data; that of the combined gneiss intervals was not as successful. Improvement in its regression coefficient from 0.01 to 0.12, though significant, was not good enough to consider it an acceptable model. This evidently has to do with the poor match of the result with measured core data as revealed in its log section. The defect-model however, failed in the white schist and granite-amphibolite correlations respectively.

It was particularly surprising to observe this failure for the white schist interval that given its near-perfect correlation result in previous standard method. Assessment of the raw data for the later rock intervals did show significant errors in the recorded values though, but there were stronger indications that the failure of the models might have to do with factors other than defects. Factors such as anisotropy, differential frequency of wave propagation and differential stress conditions were suspected to be of much greater influence to the measurements. Comparison of current model results with classic ones from published works, show a sort of dependency of the global applicability of models to rock type. Finally, good models when established for a location tend to produce much better in-situ static estimates than models foreign to the location. The model result of the granite-gneiss proved this assertion and seemed to confirm similar conclusions in some published works.

ACKNOWLEDGEMENTS

My sincere thanks to my thesis supervisor, Professor Robert Scholger, who was assigned to me on ad-hoc capacity; yet he made time out of his busy schedule to provide the best supervision I could ever wish for. His patience and insightful assitance made the timely conclusion of this work possible. I would also like to recognize the mentorship offered by the Chair of Applied Geophysics ably represented by Professor Florian Bleibinhaus. He never failed to provide prompt resolutions to my academic challenges.

My gratitude also goes to the research institute which provided the borehole log data (under the condition of anonymity) used for analysis as per location 1. And then, the Chair of Subsurface Engineering for providing results of compressive tests conducted on sample cores from the same location.

In addition, I would like to thank the secretary to the Chair of Applied Geophysics, Mrs Christiane Pretzenbacher, for granting my request to use the Geophysics lab and library facilities, particularly for requests made at odd hours. And also the research staff of the Chair; Jens Zeiss and Kathrin Peters-Poethke. I do appreciate their computing assistance.

To my friends Obinna Muoneke, Alyssa Howsmon, Shelby Billings and McKenzie Kasteler; I would say, thank you for being there.

Above all, my unreserved and immeasurable gratitude to my family for their unalloyed support and love. I want to appreciate their material and spiritual encouragements. The journey would have been a lot tougher without those. Thank you all.

TABLE OF CONTENTS

Abstract ii

Acknowledgements vi

Table of Contents vii

List of Tables viii

List of Figures ix

1: Introduction 1
1.1 Definition of terms 1
1.2 Geomechanical importance of subject 2
1.3 Objectives and scope of work 3
2: Measurement methodology 7
2.1 Borehole measurements 7
2.1.1 Full waveform sonic logging 7
2.1.2 Optical borehole imaging 9
2.1.3 Density logging 13
2.2 Laboratory measurements 14
2.2.1 Sample preparations 14
2.2.2 Composite uniaxial compressive test (Location 1) 15
2.2.3 Isolated ultrasonic measurement (Location 2) 17
3: Results and discussions 19
3.1 Data quality assessment 19
3.2 Standard correlations with raw data 26
3.2.1 Correlations for location 1 27
3.2.2 Correlations for location 2 36
3.3 Defect-model-based correlations 39
3.3.1 Derivation of model equations for location 1 41
3.3.2 Derivation of model equations for location 2 44
3.4 Application of derived model equations to log data 47
3.5 Comparison of model results with Literature 52
4: Interpretations 60
5: Conclusion 63
Appendix: Data tables and graphs 65

References 73

LIST OF TABLES

Table 3.1: Measured stress and strain values for sample core at 15.60m depth (BH 9).... 24

Table 3.2: Calculated log and laboratory dynamic values for BH 10..... 28

Table 3.3: Measured stress and strain values for sample core at 2.30m depth (BH 10).... 30

Table 3.4: Calculated standard static and dynamic Young's moduli for BH 10 31

Table 3.5: Calculated standard static (BH 9) and dynamic Young's moduli (BH 8 and BH 10)..... 34

Table 3.6: Calculated standard static and dynamic Young's moduli for the Pilot borehole (location 2)..... 36

Table 3.7: Calculated model dynamic and static properties with corresponding solid matrix factor (BH 10)..... 43

Table 3.8: Current and classic model static equations applied to dynamic log data (modified from Brotons et al. 2016)..... 53

Table A.1: Measured stress and strain values for sample core at 3.40m depth (BH 10) 65

Table A.2: Measured stress and strain values for sample core at 3.60m depth (BH 10) 65

Table A.3: Measured stress and strain values for sample core at 3.80m depth (BH 10) 66

Table A.4: Measured stress and strain values for sample core at 6.60m depth (BH 10) 66

Table A.5: Measured stress and strain values for sample core at 6.80m depth (BH 10) 67

Table A.6: Measured stress and strain values for sample core at 7.90m depth (BH 10) 67

Table A.7: Measured stress and strain values for sample core at 15.40m depth (BH 9)..... ..68

Table A.8: Measured stress and strain values for sample core at 15.80m depth (BH 10) 68

LIST OF FIGURES

Figure 2.1: Schematic diagram showing makeup of the Sonde probe for sonic logging 8

Figure 2.2: Typical wave train as recorded at the receiver units of a sonic log Sonde probe 9

Figure 2.3: Diagram showing makeup of Sonde probe for an Optical Borehole Imaging (OBI) device 10

Figure 2.4: A feature cutting across a borehole as it would be seen on flat-surface OBI log section (Williams et al. 2004) 11

Figure 2.5: Feature cutting across a borehole produces a mirror symmetry in its OBI log section (Zemanek et al. 1970) 12

Figure 2.6: Photo and schematic image of apparatus used for the composite uniaxial compressive test (Gegenhuber et al. 2017) 15

Figure 2.7: (a) Illustration of typical deformation by compression. (b) axial and radial strain curves for a uniaxial compressive test (Schoen 2015) 16

Figure 2.8: Photo showing the apparatus for ultrasonic laboratory velocity measurements (Pittino et al. 2016) 18

Figure 3.1: Plot of calculated dynamic moduli against depths (BH 10 at location 1) 20

Figure 3.2: Log section comparing OBI log with FWS log for the white schist interval (BH 10) 20

Figure 3.3: Stress-strain response of rock intervals at depths (BH 10) 21

Figure 3.4: (a) Plot of calculated dynamic moduli against depths (BH 8). (b) A section of plot zoomed-in 23

Figure 3.5: Stress-strain plot showing unusual loading and unloading sessions (15.60m depth, BH 9) 25

Figure 3.6: Log and laboratory dynamic moduli plots for (a) granite-gneiss. (b) white schist 29

Figure 3.7: Stress-strain plot showing typical loading and unloading sessions (2.30m depth, BH 10) 31

Figure 3.8: Standard static-dynamic regression plots for (a) granite-gneiss. (b) white schist 32

Figure 3.9: Plot of Dynamic-static ratio against static moduli, compared with model by Schoen 2015 (top) 33

Figure 3.10: Regression plots using static data from BH 9 against dynamic log data from BH 8 and BH 10 35

Figure 3.11: Regression plots for all rock types in the Pilot borehole at location 2 37

Figure 3.12: Regression plot for all the gneiss bearing intervals in the Pilot borehole 38

Figure 3.13: Calculated solid matrix factor (A) based on velocity type (a) for granite-gneiss. (b) for white schist 42

Figure 3.14: Defect-model regression plots for granite-gneiss and white schist respectively 44

Figure 3.15: Calculated solid matrix factor (A) based on Vs (a) for all gneiss intervals in the Pilot borehole. (b) for granite-amphibolite 45

Figure 3.16: Defect-model regression plots for the combined gneiss intervals and granite-amphibolite respectively 46

Figure 3.17: Log section comparing model result with dynamic log data (granite-gneiss) 48

Figure 3.18: Log section comparing model result with dynamic log data (white schist) 49

Figure 3.19: Log section comparing model result (BH 10) with dynamic log data of BH 8 49

Figure 3.20: Log section comparing model result with dynamic log data (combined gneiss intervals at location 2) 50

Figure 3.21: Log section comparing model result with dynamic log data (granite-amphibolite) 51

Figure 3.22: Comparison of current model with classic models for granite-gneiss using regression plot (top) and log section (bottom) 55

Figure 3.23: Comparison of current model with classic models for white schist using regression plot (top) and log section (bottom) 56

Figure 3.24: Comparison of current model with classic models for the combined gneiss intervals in the pilot borehole using regression plot (top) and log section (bottom) 58

Figure 3.25: Comparison of current model with classic models for granite-amphibolite using regression plot (top) and log section (bottom) 59

Figure A.1: Stress-strain plot showing only the loading session (3.40m depth, BH 10) 69

Figure A.2: Stress-strain plot showing only the loading session (3.60m depth, BH 10) 69

Figure A.3: Stress-strain plot showing only the loading session (3.80m depth, BH 10) 70

Figure A.4: Stress-strain plot showing only the loading session (6.60m depth, BH 10) 70

Figure A.5: Stress-strain plot showing only the loading session (6.80m depth, BH 10) 71

Figure A.6: Stress-strain plot showing only the loading session (7.90m depth, BH 10) 71

Figure A.7: Stress-strain plot showing loading and unloading sessions (15.40m depth, BH 9) 72

Figure A.8: Stress-strain plot showing loading and unloading sessions (15.80m depth, BH 9) 72

1: INTRODUCTION

1.1 Definition of terms

Young's modulus refers to a modulus of elasticity which measures the stiffness of a material. In the present context, it is a measure of a material's resistance against being compressed or stretched by a uniaxial stress. The resistance offered is usually in the form of withstanding changes in length, when under lengthwise (uniaxial) tension or compression. Therefore, Young's modulus can also be referred to as the *ratio of the change in longitudinal or axial stress, to the change in longitudinal or axial strain*; where stress represents the compressional or tensional force and strain represents the lengthwise deformation. In ideal situations, Young's modulus of a material is constant because the axial stress produces proportional axial strain, and the sample returns to its original dimensions when the external compressional or tensional force is removed. However, this is not usually the case for geological materials such as rocks. For most rocks, as the stress increases, Young's modulus no longer remain constant but usually decreases because the strain increases disproportionately. This is due to permanent deformations of parts of the rocks, which then do not return to their original dimension when the stress element is removed. Fjaer et al. (2008) associates this permanent deformation with a release of potential energy otherwise known as the *strain energy*, during the withdrawal or unloading of the stress element. For Young's modulus determined through seismic wave propagations, Zisman (1933) attributed this energy release or rather energy loss to reflection and refraction effects suffered by the propagating wave pulse at the fluid/rock interfaces (intergranular pores and natural fractures). The stated condition of permanent deformation is referred to as *non-linear elasticity*; while the ideal case described earlier is said to be *linearly elastic*. Further more, there may also be a decrease in strain as the stress increases. This is in part due to closure of cracks and microfractures in the sample material at sufficiently high stress conditions. In fact, at very high stresses, the sample assumes a perfect solid composition devoid of pores (cracks,fractures e.t.c); thus resulting in increased Young's modulus of elasticity. This also explains the observed increase of Young's moduli with increasing hydrostatic pressure (increasing depth), in most formations. Exceptions however, do exist. Shaly or mud rocks may deviate from this general conception, as they show high unpredictability for elastic properties.

Young's modulus of materials can be influenced by the lattice orientation of their constituent particles, usually refered to as their *isotropic state*. Ideally, the linear stress-strain relationship as discussed earlier is assumed to be for an isotropic and homogenous condition. For most rock types this is again, not the case. Rocks are usually anisotropic to some extent, owing to their heterogenous compositions; including the presence of cracks. According to Fjaer et al. (2008), when the anisotropy is due to lithological differential composition, it is refered to as *intrinsic anisotropy*. And when it is resulting from cracks and similar features, it is refered to as *stress induced anisotropy*. Over all, both types introduces error in the determination of Young's modulus. Unfortunately, it is ignored in rock elasticity calculations, because its description requires more information about the material, which are not usually available.

Young's modulus can be measured both in the laboratory by compressive test techniques and also from in-situ borehole logging. When the measurement is acquired in the laboratory compressive tests, the property is refered to as *static Young's modulus*. And when acquired from borehole logs, it is termed *dynamic Young's modulus*. Dynamic modulus can also be determined in the laboratory through ultra seismic wave propagation procedures.

1.2 Geomechanical importance of subject

In engineering and construction projects, determination of the Young's modulus is very crucial because it indicates deformational characteristics of rock types encountered in such project (McCann and Entwisle 1992). While some engineers make do with deformational information from analysis of rock strength properties like the uniaxial compressive strength (UCS), most prefer deformational information from elastic property analysis like the Young's modulus. This is possibly because estimation of static Young's modulus for example, allows for detailed analysis of deformational responses to variable stress regimes, a feat not exactly possible if only uniaxial compressive strength is to be estimated.

Elkatatny et al. (2017) asserted that determination of the Young's modulus especially for specific rock type in a given formation, is essential in building a geomechanical model that can be applied in operations involving mechanical rock failures such as; well drilling, well completion, wellbore stability, estimation of formation breakdown pressure and fracture stimulations. Hongkui et al. (2001) stated that the dynamic Young's modulus albeit being the less preferred in engineering works, is simple, time/cost-saving in measurement; and gives a continous elastic parameter profile under in-situ conditions. Laboratory measurement of Young's modulus and subsequent applications to in-situ stress fields is gradually replacing the in-situ loading tests (vertical load tests) in many geotechnical investigations, due to the hugely destructive nature of the later method.

1.3 Objectives and scope of work

The primary objective of this work is to compare and correlate the two measurement approaches (static and dynamic) for the elastic Young's modulus of rocks; then validate the correlations by establishing model-based relationships that can be applied to log data of not just the chosen measurement borehole, but also log data of adjacent and nearby boreholes. The model correlations would be compared with similar works from literature to ascertain whether the results could be deemed satisfactory or not. The objective is also to investigate some assertions in the literature explaining the discrepancy between dynamic Young's modulus measured in the laboratory using ultrasonic wave pulses on core samples, and that derived from in-situ full waveform sonic log data. And lastly, an investigation of possible difference in the properties measured in the laboratory by adopting a newer composite uniaxial compressive measurement technique; compared to adopting the older and conventional isolated measuremnts. The composite uniaxial compressive measurement here, simply refers to uniaxial compressive test involving *simultaneous measurement of the dynamic and static properties under the same set-up and conditions*. The usual practice has been to carry out the acoustic wave measurements using separate apparatus from the set-up for the static compressive tests.

Pittino et al. (2016) concluded that the composite set-up with the integrated probes ensures better and more accurate determination of the compressional and shear wave velocities at different stress-strain regimes.

And that conclusions can be drawn on in-situ stress conditions based on this additional functionality.

The measurements were already taken and resulting data made available for this work. However, standard measurement procedures for only the parameters of interest in subsequent analysis, would be discussed. After a quick assessment of the quality of data provided for the measured parameters; the dynamic Young's modulus would be calculated first from the compressional (V_p) and shear (V_s) wave velocities, as well as the density data. The velocity data would be extracted from the full waveform sonic logs, while the density data would come from the density logs. The static Young's modulus would then be determined from the compressive test results using the tangent-modulus-method. This method requires that the slope of the tangent to the stress-strain curve be determined at a position corresponding to about 50% of the ultimate stress before unloading; or 50% of the uniaxial compressive strength (UCS) in the case of compression till fracture. The determined slope of the tangent gives static Young's modulus. The tangent-modulus method was only applied using measurements from location 1, as they involved stress loading and unloading sessions. The second location on the other hand, had the static modulus already computed from UCS and made available for further analysis. The static data derived from these methods would then be crossplotted with the dynamic data to establish possible correlation or otherwise. It has been proven in most literary publications that there exist significant discrepancy in values between the static Young's modulus measured in the laboratory and the dynamic Young's modulus calculated from log data. Schön (2015) attributed this discrepancy to the difference in stress-strain magnitudes as measured by the dynamic and static approaches. While the dynamic (seismic wave propagation) technique exerts smaller stress and generates smaller strain, the static (compressive test) technique involves larger stress and strain. He also stated, in agreement with McCann and Entwisle (1992), that the discrepancy can also be attributed to partial non-elastic deformations during static measurements, possibly due to mobilization of microcracks, pores and grain contacts. Elkatatny et al. (2017) supports this proposition of microcracks influence, especially under high stress.

They posit that the discrepancy is more pronounced in softer rocks than harder rocks, or as Schön (2015) puts it; that the discrepancy decreases from unconsolidated (low velocity) sediments to compact (high velocity, non-fractured) sediments. Fjaer et al. (2008) stated that the major reason for the discrepancy is the difference in strain amplitude (extent of deformation) and not strain rate (rate of deformation) between the two approaches. They concluded that the large strain amplitude (10^{-3} to 10^{-2}) of static moduli which are measured as slopes of stress-strain curves, differ from the small strain amplitude (10^{-7} to 10^{-6}) of the dynamic moduli because of plasticity effects. It is important to note however, that these discrepancies does not connote lack of correlation in any way. In fact, correlations has not only been established for the static-dynamic data measurements with widely different values; but also for static against velocity or density parameters normally used in calculation of the dynamic property, and whose values are in no way comparable. The work of Elkatatny et al. (2017) centered on using this type of correlation to derive model static correlation equation, given the failure of the direct static-dynamic correlation in their location of investigation. Kassam et al. (2016) used the correlation of static modulus with compressional and shear wave velocities to calculate density of rocks traversed by a borehole. They concluded that this approach could help eliminate density logging operations entirely in geomechanical property investigations, given the associated environmental concerns (use of radioactive materials for density logging). Hongkui et al. (2001) proposed a linear relationship for their static-dynamic correlations, and put the static/dynamic ratio at 0.6. Mockovcjakova and Pandula (2003) argued that correlations are only valid for homogenous and isotropic media, and therefore fails when applied simultaneously to sequence of varying rock types. Eissa and Kazi (1988) on the other hand, considered wide range of rock sequences and still came up with a strong correlation with regression coefficient of 0.70.

The dynamic calculations would also be carried out for velocities measured in the laboratory by ultrasonic means. For the first location, this laboratory dynamic data which is measured simultaneously with the static compressive test would be compared with the dynamic data from the full wave sonic logs.

Fjaer et al. (2008) argued that there is discrepancy between the laboratory and log measurements of the dynamic Young's modulus. This they stated, is due to different stress conditions for the two measurement environments. They believe that even if the downhole conditions are replicated in the laboratory, *stress relief* which has become extremely difficult to measure in the borehole can still cause significant diffference in the two measurements. More importantly is their strong conviction that different frequencies of wave propagation in the borehole and in the laboratory, do cause more of the discrepancy than the differential stress conditions. They concluded that the laboratory measurement will always produce higher dynamic Young's modulus than that from in-situ velocity logs.

To establish the effectiveness or otherwise of the simultaneous measurement of the static and dynamic properties, a correlation of these two properties measured in the laboratory would suffice; and would then be compared with similar correlation for isolated or separate measurements of the same properties.

Due to the effect of cracks and pores on all the laboratory-measured values, a simplified defect model as proposed by Schön (2015), would be applied to establish model relationships which have been corrected for such effects. Gegenhuber et al. (2017) applied the same principle and showed good results for a UCS-V_p correlation. Established defect-model correlation equations would be applied on log data and the fitness visualised in the form of traces. Also, the optical image log data made available would be used to corroborate zones of significant defect as may be reflected by resulting models. Finally, interpretations would be made, based on observed correlation results as well as defect trends in different rock types; and conclusions drawn from them.

2: MEASUREMENT METHODOLOGY

2.1 Borehole measurements

2.1.1 Full waveform sonic logging

Full waveform sonic (FWS) logging otherwise called full waveform acoustic logging, provides information about seismic and lithologic properties of a formation. It is different from the conventional acoustic logging in that, while conventional acoustic logging measures only compressional (P-wave) travel time through the borehole walls; FWS logging measures all the seismic wave train (compressional, shear and stoneley). The tool for FWS logging is much similar to the conventional acoustic logging, except that the source for the former is usually of low frequency and it's source-receiver distance is longer. FWS logging tools measure the slowness (inverse velocity or time needed to travel a fixed distance) of refracted arrivals in much the same way as the conventional acoustic logging. This is accomplished by picking their signal arrivals, using a threshold detection algorithm, and also measuring the move-out between receivers if more than one receiver (or an array) are used. In the order of their arrival time, P-wave is picked first, then the shear wave and lastly the stonely wave. In soft formations, picking of the shear wave arrivals may be difficult or totally impossible, especially if the shear wave velocity is lower than the acoustic velocity of the borehole fluid. In this case, shear wave slowness can be indirectly estimated using the stoneley wave slowness (Stevens et al. 1986). However, Burns et al. (1988) and Williams et al. (1984) argued that a number of factors like permeability could affect stoneley wave slowness, and went ahead to recommend direct shear wave logging tool as the only reliable method. McCann and Entwisle (1992) on the other hand suggested the application of the Christensen's equation (shown below) in calculating for shear wave velocity.

$$V_s = V_p \left[1 - 1.15\left(\frac{{}^{1}/_{\rho} + {}^{1}/_{\rho^3}}{e^{{}^{1}/_{\rho}}}\right)\right]^{{}^{3}/_{2}}$$ where ρ is formation density.

They however, did note that this equation gives an over-estimate of the shear wave velocity in mudrocks and soft sediments, and therefore will increase the corresponding dynamic moduli calculated with it (Entwisle and McCann 1990).

Castagna et al. (1985) also derived an empirical relationship for calculating the shear wave velocity when only the compressional wave velocity is known, thus;

$$V_s = 0.8621 * V_p - 1.1724 \quad \text{where } V_s \text{ and } V_p \text{ are in kms}^{-1}.$$

Schön (2015) insisted that these equations are purely empirical and are only valid for specific formations.

The FWS tool consist of a sonde probe housing two ultrasonic transmitters and two ultrasonic receivers; which is attached by means of a cable to a roller winch placed in a logging truck (figure 2.1). The transmitters produces wave pulses that propagates to the borehole walls and are refracted and/or reflected. The refracted/reflected pulses are picked up by the receivers and transmitted through the coaxial cable to the recording unit in the logging truck. This process is continous as the sonde is pulled up or down the borehole.

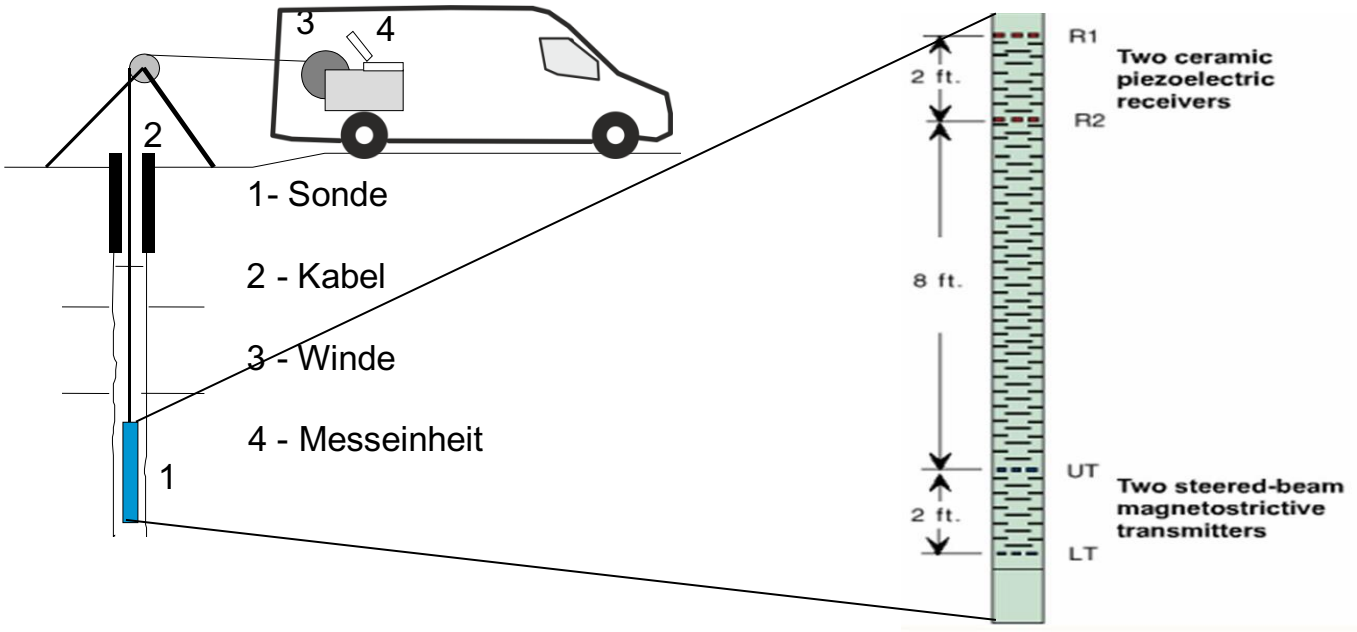

Figure 2.1: Schematic diagram showing makeup of the sonde probe for sonic logging

The sonde probe is centered in the borehole by a special centering device coupled to it. From the data made available for current study, targeted hole diameter was 75-300 mm at location 1 and 165-445 mm at location 2, and corrections for possible cave-ins in the borehole walls were carried out using the caliper log.

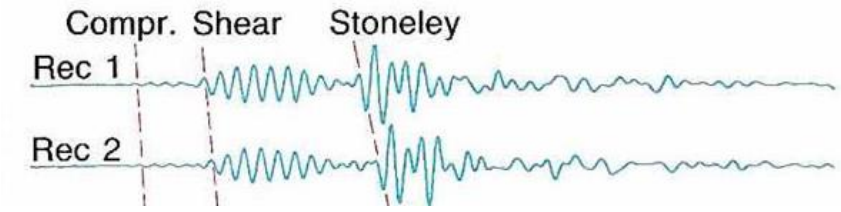

Figure 2.2: Typical wave train as recorded at the receiver units of a sonic log sonde probe

With vertical resolution targeted at 20cm, the signals of interest (V_p & V_s) were picked,digitized and uploaded unto the WELLCAD interpretation software (see figure 2.2). The software tabulated the data in an exportable excel format and also plots them as a function of depth down the borehole in log curves or wave patterns, ready for analysis.

2.1.2 Optical borehole imaging (OBI)

This is a borehole logging system that generates a continous oriented 360^o image of the borehole wall using downhole CCD (charge-coupled device) camera. The tool for the measurement is in form of a probe much like other downhole logging tools but consisting of the CCD camera, a ring of lights to illuminate the borehole for the camera and a conical or hyperbolic reflector (prism) housed in a transparent cylindrical window (figure 2.3). The prism allows 360^o slices of the full borehole wall to be recorded. Orientation of true color image of the borehole wall is achieved with the help of a three-axis magnetometer and a three-axis accelerometer inside the probe. The entire components are coupled inside the probe (sonde-like jacket), attached to a cable for lowering into or pulling out of the borehole. Centralisation for the probe itself is achieved by using two spring centralisers located towards the top and bottom of the probe.

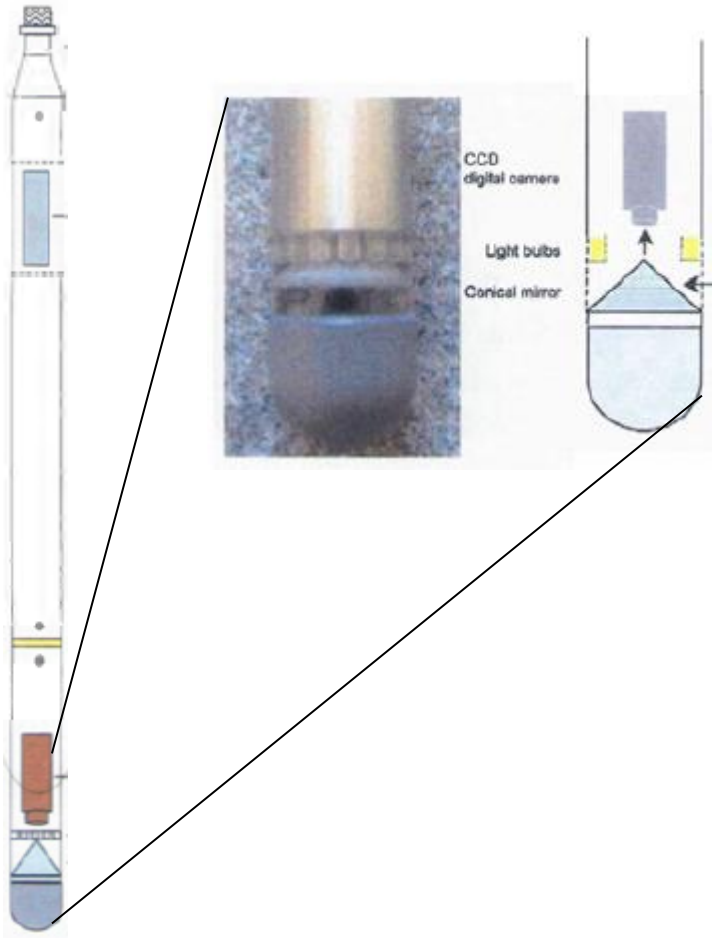

Figure 2.3: Diagram showing makeup of sonde probe for an Optical Borehole Imaging (OBI) device

Optical borehole imaging is the oldest form of borehole inspection using images, and is quite diffrent from the acoustic borehole imaging. It provides direct view of the borehole walls in clear water-filled or air-filled down-hole conditions. This condition of having clear and visible conditions in the borehole makes it a less prefered option to the acoustic imaging technique which can even be used in drilling operations involving mud. However, the former can show better images of lithology, planar and fracture features than the acoustic technique. Williams and Johnson (2004) therefore proposed a complementary use of these two image logs, and showed how effective this approach could be in interpretation of down-hole images.

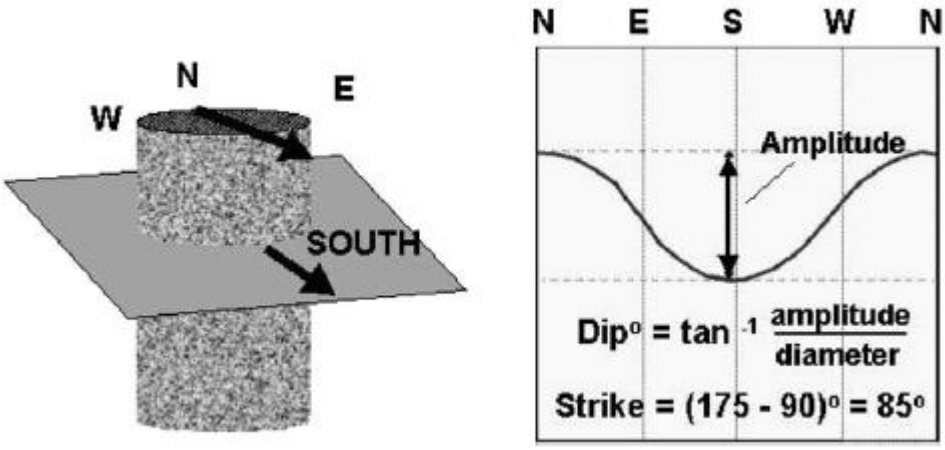

Figure 2.4: A feature cutting across a borehole as it would be seen on flat-surface OBI log section (Williams et al. 2004)

They also showed how to calculate dip and strike of a non-vertical planar feature cutting across the wellbore, by inspecting the optical image log which is usually represented as if the borehole is split vertically along magnetic north, unfolded and laid flat (figure 2.4). The dip is then calculated from the amplitude of the sinusoidally-shaped representation of the feature on the image log. This conforms with the illustrations of Zemanek et al. (1970), who also showed that if such feature cuts the wellbore vertically, the log representation would be mirror image of each half of the feature in the borehole (figure 2.5). Zemanek therefore concluded that one gains confidence that an observed feature cutting the wellbore is real if it possess mirror symmetry in its image log representation.

OBI measurement for current work is much similar to the FWS set-up described earlier, except for the use of sonde with different components. Target vertical resolution was 1 mm translating to about 720 pixel per line data. It also implies logging speed was kept below 3 m/min to achieve this resolution. The sonde simultaneously transmits multiple slices of the photographed borehole wall through the coaxial cable to the measuring unit in the logging truck. It is important to note that the OBI was only carried out in location 1.

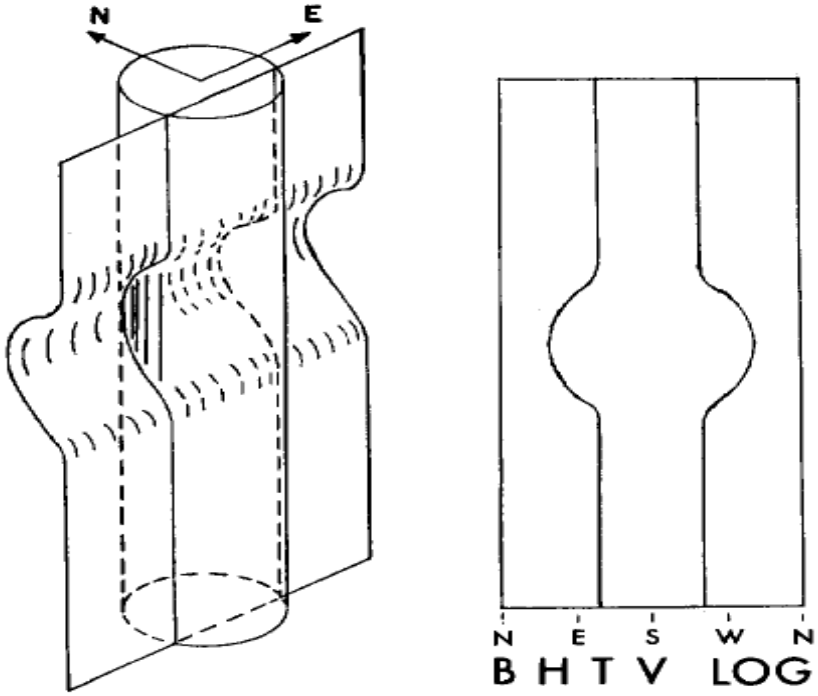

Figure 2.5: Feature cutting across a borehole produces a mirror symmetry in its OBI log section (Zemanek et al. 1970)

Possible reasons for not using same in location 2 being that the pilot borehole at the location has wider diameter (445 mm) at shallow depth than the optimal or maximum recommended for this kind of imaging operation (Williams and Johnson, 2004.). Another possible reason is that unlike the few meter depths involved in location 1, the depths in location 2 runs into thousands of meters. And Prensky (1999) stated that at such great depths (> 5000 ft), the quality and resolution of downhole images are adversely affected by high pressures and temperatures. Limited use would be made of the OBI images during analysis because the depth intervals where samples were collected for the elastic property analysis in this work were devoid of fractures, as is the practice. However, it would be useful in analyzing lithological boundaries and to a lesser extent intervals with microcracks, which may give an idea of the tectonic processes in the location.

2.1.3 Density logging

Density logging like other downhole logging operations provides continous record but of formation's bulk density instead, along the length of a borehole. The bulk density being a function of the minerals forming a rock (matrix) and the fluid enclosed in the pore spaces. Typical tool for this measurement consists majorly of a radioactive source and a detector, both of which are lowered down the borehole. The radioactive source is usually of Caesium (Cs-137) element. In the borehole, the source emits medium-energy gamma rays into the formation. These gamma rays interact with electrons in the formation and are scattered in the process refered to as *compton scattering*. The number of scattered gamma rays that reach the detector, placed at a set distance from the source, is related to the formation's electron density (ρ_e); which in turn is an indication of the formation's bulk density (ρ_{bulk}), and are related thus:

$$\rho_e = 2\rho_{bulk}\frac{Z}{A}$$

Where Z is the atomic number, and A is the molecular weight of the compound. For most elements, the ratio $\frac{Z}{A}$ is 0.5 except for hydrogen which is 1. The electron density (ρ_e) in the formation determines the response of the density logging tool. Recent designs of the logging tool possess multi-detector (2 or more detectors) functionality, where short-spaced detector(s) are introduced to record shallower depth emissions. Thus, they provide indications of the drilling fluid influence. Also, the shorter-spaced readings can be used to correct the longer-spaced detector(s) which records emissions deeper into the formation walls.

Porosity can be inferred from density logging if one knows, in addition to the measured bulk density, matrix density and the density of fluid in the pores.

This is the most important application for density logging, and one of the three possible means of in-situ porosity assessment. The other two being by sonic logging and neutron-porosity logging. For location 1, no density logging was carried out. An empirically determined value of 2.7 gcm^{-3} was used for the entire borehole length. This is based on the fact that depth intervals here are in fractions of a meter and maximum depth is just a few tens of meter; hence it is believed that there would not be any significant change in the average bulk density.

Location 2, on the other hand has density logs and records of intervals of interest were extracted accordingly. It was also not uncommon to see contrasting values in the record for the same rock type or unit, sometimes much lower than the expected average for such rock type. This is assumed an indication of bad data or anisotropic effect, and were removed before further analysis.

2.2 Laboratory measurements

2.2.1 Sample preparations

The ISRM (International Society for Rock Mechanics) standards demands that rock specimens to be used for mechanical tests be flat-top, circular cylinders with length to diameter ratio between 2:1 and 3:1. Fjaer et al. (2008) stated that the reason for this choice of dimension is to make the sample sufficiently long to accomodate a shear plane penetrating through the side walls, which otherwise would penetrate through the end faces. Typical size of drilled cores for current investigation is 10cm diameter and 20cm length. Special care was taken to ensure that the plugs or cores were drilled absolutely normal to bedding planes. This is because strength of rocks are at the minimum when drilled at angles oblique to bedding planes. Also, the outer centimeters of the rock samples were avoided during drilling, as they are usually invaded by the drilling mud, and therefore their strength are already compromised. The samples were assumed completely drained even when they may not be, because in principle, the compressive tests discharges whatever fluid component in the pores of the cores by the action of compression. An exception to this, is the isolated dynamic laboratory measurement of location 2, where the samples used in that case were thoroughly dried to maintain uniform saturation condition as in the compressive test situation.

It is very important to note here that all the core samples were taken from intact rock intervals with almost no visible fractures. However, most of them might have undergone some form of stress relief or release (Fjaer et al. 2008), and might have been chemically altered during handling and transportation. Therefore the eventual analysis is subject to errors introduced by these inadequacies and may not be a true representation of the entire in-situ rock mass.

2.2.2 Composite uniaxial compressive tests (Location 1)

This technique allows for simultaneous measurement of elastic wave velocities as a sample core undergoes compressive test. Typical apparatus used for this measurement is the so-called servo-hydraulic testing machine MTS 815, equipped with integrated probes (P) for velocity measurements, and then the normal sensor-ridden compression platens for determining axial deformational changes at variable stresses (figure 2.6). The velocity probes from the company "Geotron Elektronik" (Pirna, Germany) were constructed in such a way as to protect them from the high compressive forces.

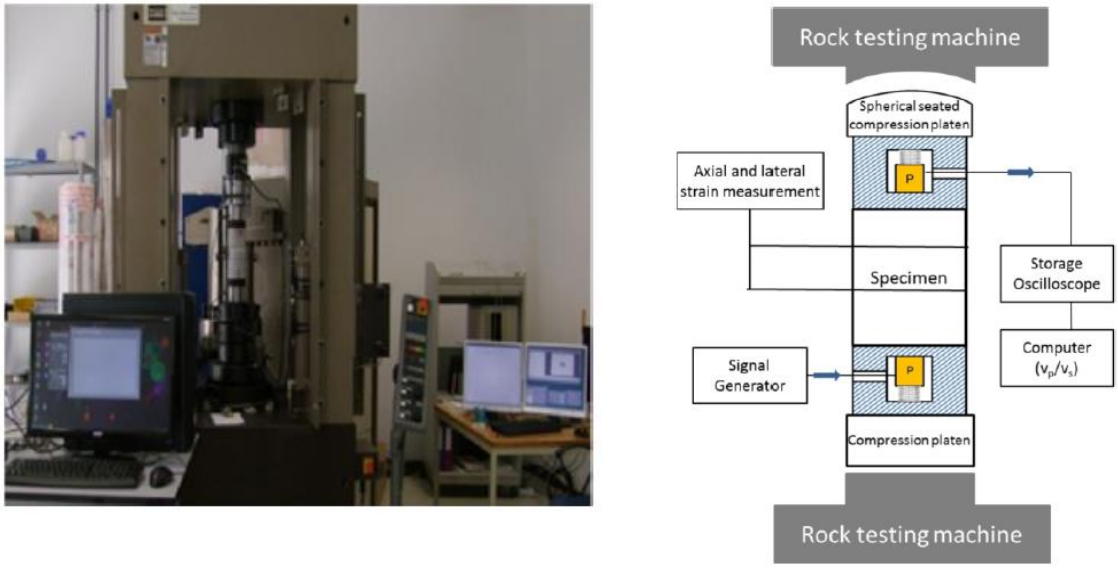

Figure 2.6: Photo and schematic image of apparatus used for the composite uniaxial compressive test (Gegenhuber et al. 2017)

The cylindrical sample is placed between the compression platens with the integrated velocity probes as shown in figure 2.6. It's initial length is recorded.

For each unit of force (stress) applied through the compression platens, the axial strain (change in length relative to the initial length) was recorded; and then ultrasonic signal is generated at the lower probe and transmitted through the sample to the upper probe, which in turn sends the received signal to a storage oscilloscope, and finally to a computer for display and picking of the arrival times (slownesses) of the different wave velocity components. Increasing force (stress) regimes are applied and the process repeated each time.

In the case of data provided for current work, upon achieving a maximum force of 500 KN (translating to stress of approximately 60 MPa), the applied force is gradually withdrawn while measuring the step-wise velocities and strains at withdrawal. The gradual increment of force (stress) is termed the *loading session* and was used in determining static Young's modulus; while the gradual withdrawal is termed *unloading session*. Note that this combined measurement with loading and unloading sessions was only carried out for location 1, as the objective was never to compress the sample to total fracture or crumbling. Location 2 was entirely of the conventional loading and compression till total fracture or crumbling (figure 2.7a), and also without simultaneous measurement of the velocity properties. The isolated measurement for the velocities in the later location will be discussed in the next section.

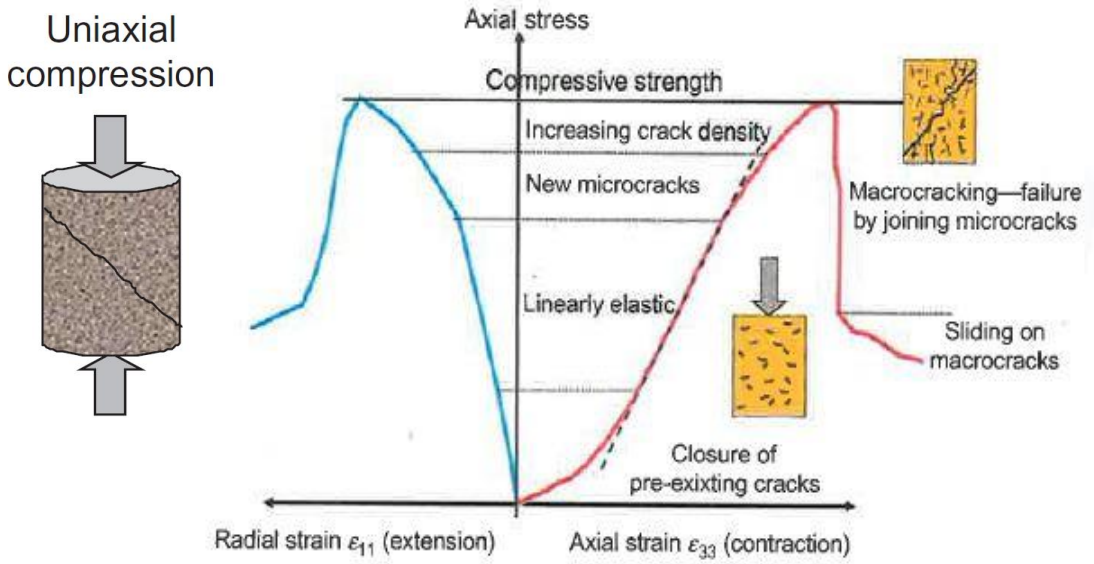

(a) (b)

Figure 2.7: (a) Illustration of typical deformation by compression. (b) axial and radial strain curves for a uniaxial compressive test (Schön 2015)

This also means that, while the peak or ultimate stress of the loading sessions before withdrawal was used in calculations for location 1, the UCS value obtained at total crumbling of a sample was used for location 2.

Typical stress-strain curve for a compressive test technique with or without simultaneous velocity measurements is as shown in figure 2.7(b). The tangent modulus method was used to calculate the static Young's moduli from the curve. This method establishes a tangent to the stress-strain curve at a position corresponding to 50% of the peak or ultimate stress (in the case of the loading sessions), or 50% of the UCS (in the case of compression till rupture). The slope of the tangent then becomes the desired static Young's modulus.

In both locations, dynamic Young's moduli would be calculated using the measured P-wave and S-wave velocities and equivalent densities by applying the formular below;

$$\boldsymbol{Dynamic\ Young's\ modulus} = \boldsymbol{\rho V_s^2 \left(\frac{3V_p^2 - 4V_s^2}{V_p^2 - V_s^2}\right) . 10^{-6}} \quad \text{..... (1)}$$

Where the dynamic Young's modulus is in megapascal (MPa), V_p and V_s are P-wave and S-wave velocities in meter per second (m/s) respectively, ρ is the bulk density in kilogram per cubic metre (Kgm^{-3}).

2.2.3 Isolated ultrasonic measurement (Location 2)

The basic principle behind this measurement is the generation of electric field when external voltage is passed through piezo-electric transducers. Two piezo-electric transducers are usually placed between pistons or compression platens holding the core sample, as in the compressive test. The top transducer generates singular mechanical pulse of frequency of about 80 KHz which is transmitted through the sample and unto the lower transducer. The lower transducer becomes deformed by the alternating voltage generated from the received signal and generates pulse wavelets or oscillations too. The oscillations are then stored as waves in an oscilloscope and further transmitted unto a computer screen for visual analysis. The arrival times of the waves are also recorded by the computer and velocities automatically calculated from them given the known length of the sample between the transducers (pistons).

Figure 2.8: Photo showing the apparatus for ultrasonic laboratory velocity measurements (Pittino et al. 2016)

It follows therefore, that the initial travel or transit time of such wave be recorded when there is no sample yet between the transducers, to serve as the basis for calculating relative travel time when the sample is finally in place. This initial travel time is called the *dead time*. The difficulty is usually in picking the first arrivals from the different velocity components. In current case, a self-developed program (Gegenhuber and Steiner-Luckabauer 2012) was applied in picking the P-wave and S-wave arrivals with little difficulty. The values were tabulated and used to calculate corresponding dynamic Young's moduli. The set-up is as shown in figure 2.8.

3: Results and discussions

3.1 Data quality assessment

The set of data received from both the log and laboratory measurements were critically assessed to identify and remove possible bad data that could introduce errors in the analysis. Figure 3.1 show a plot of dynamic Young's moduli derived from the FWS log data of borehole 10 as a function of only cored depth intervals. Two rock types were identified in this borehole namely; granite-gneiss and white schist. Generally, one would expect a rightward shift in the plotted data points as depth increases, signifying increasing modulus due to compaction. A true and consistent trend could be observed for the granite-gneiss interval whose moduli increases with depth. However, that of the white schist show a general decreasing trend. And also there was this huge drop in modulus value from 6.6m to 6.8m depth, which then increases slightly again at 7.9m. A look at the optical borehole image log (figure 3.2), show no visible deformational feature to account for this drop in value at approximately 6.8m depth. The white schist interval is below the uppermost granite-gneiss interval between roughly 6.4m and 9.4m depth. Note the dark to greyish-white lithological color change from 6.2m to 6.4m marking the transition. Also, the caliper log (green trace) showed no change in borehole diameter. However, the adjoining P-wave (blue) and S-wave (red) velocity traces indicated the same drop. It is safe therefore, to assume an anisotropic effect in play at this depth. And surely this would affect the calculated dynamic Young's modulus in no small way, as the property depend largely on measured velocity values. Data from the laboratory compressive tests were equally assessed based on the stress-strain relationship plots, followed by comparison of laboratory and log dynamic measurements at sampled depths and for corresponding rock types. From the plot in figure 3.3, application of about 5 MPa stress produced little or no significant strain on the granite-gneiss but did yield reasonable deformation on the white schist facies. As the stress increased to about 60 MPa, significant strains were then recorded, which is again most prominent for the white schist facies (in orange circle). This is in accordance with the expectation that white schist which is usually a product of sedimentary layered mudstone and evaporite metamorphism, can be compressed more or further than the granite-gneiss, a metamorphic product of relatively harder igneous rocks.

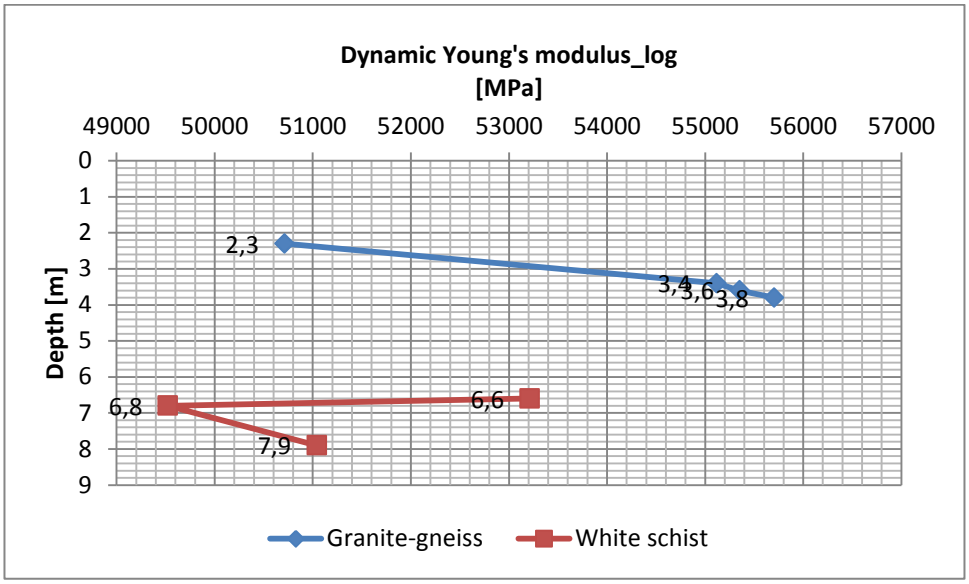

Figure 3.1: Plot of calculated dynamic moduli against depths (BH 10 at location 1)

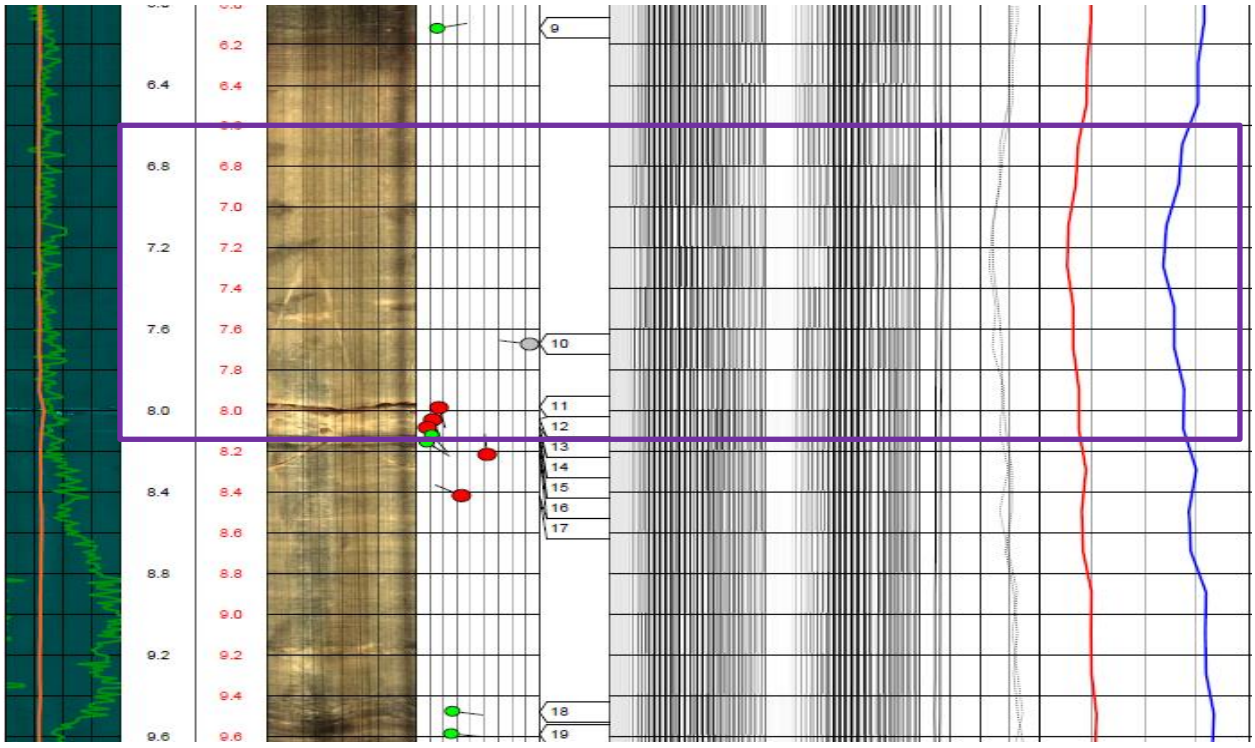

Figure 3.2: Log section comparing OBI log with FWS log for the white schist interval (BH 10)

However, a closer look at each rock facie reveals an anomalous trend in the white schist plots. In principle, deeper seated rocks should be harder and more resistant to further deformation during compressive test than shallower ones. This is simply due to overburden compaction, diagenetic and subsidence actions that had supposedly impacted on them at deeper crust over time. It implies therefore, that samples collected at greater depths ought to appear to the left of our plots signifying less strain (more resistance to deformation); while those collected from shallower depths should appear to the right at relatively higher strains (less resistance to deformation).

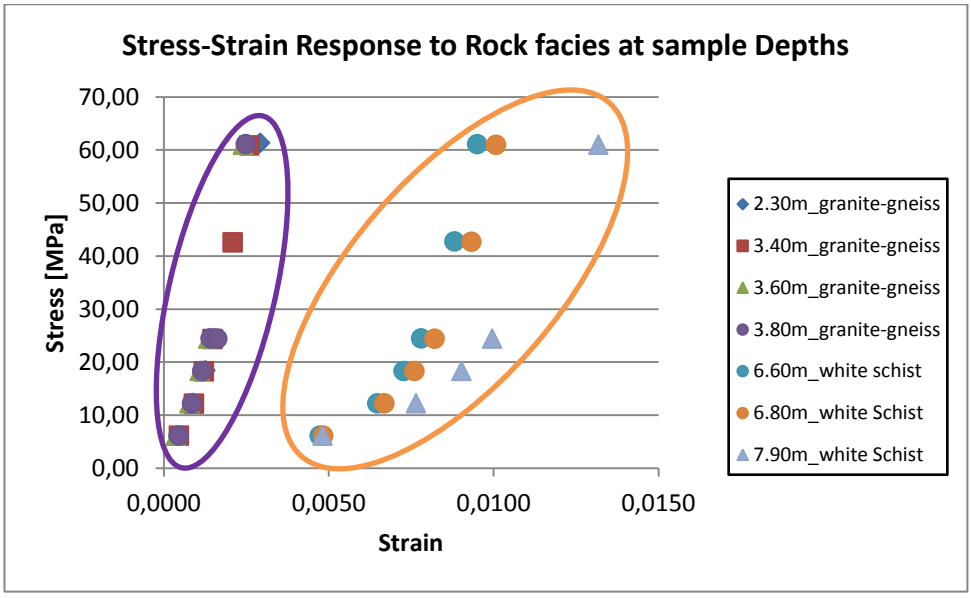

Figure 3.3: Stress-strain response of rock intervals at depths (BH 10)

Only the granite-gneiss data conformed to this rule, and can be said to be of good quality. The observation is also consistent with its corresponding dynamic data reviewed earlier, which suggested an increasing Young's moduli with depth. The white schist on the other hand, suggested increasing deformation (decreasing moduli) with depth. An interesting observation here is the fact that the data points between 6.6m and 6.8m depths are now in accord with the observed steady decreasing trend. A different development when compared with the dynamic log data of the same rock interval discussed earlier. Hence the dynamic measurement for data point 6.8m is once more confirmed bad or inconsistent by this development.

Overall, the reversed trend exhibited by the white schist could be explained if one consider that regional metamorphism is usually associated with significant tectonic events. These events do result in upturn of rock sequences sometimes leaving a seemingly younger but older (harder) rock at the top or shallower crust. Another important observation is in table 3.2, which compares the dynamic measurements from in-situ logging and laboratory test. As proposed by Fjaer et al. (2008), the expectation was that dynamic moduli measured from the laboratory tests should be higher than that from the FWS log data. This was not the case for corresponding measurements at 7.9m depth. The log value was seen to be higher in the table. Taking another look at the optical borehole image log in figure 3.2, it did reveal a major fracture a bit deeper than 7.9m (at approximately 8m depth). And one would expect the log measurement to be lower at this point compared to preceding depths. Unfortunately, it was not. Therefore, there has to be some material anisotropy between 6.8m and 7.9m depths to explain the observed decrease and increase in log values between these depths. Once again, having this occur in the white schist interval is believed to have worsened its data quality.

Only FWS log data was available for Borehole 8. This showed reasonably good quality for equivalent shallower depths as considered in borehole 10 (see figure 3.4a and 3.4b). A general trend of increasing and fairly consistent moduli can be observed in the plot, especially at the shallower portion. The logging company confirmed the same rock facie (granite-gneiss) as in borehole 10 at depths shallower than 20m, and then a diorite-hornblende-gneiss assemblage beyond 20m depth. Borehole 9 has just the laboratory compressive test data, and unfortunately one of its static measurements was marred with error, the source of which could not be ascertained. Table 3.1 show the stress and corresponding strain values recorded for this measurement. One could see the steady increase of strain during the loading session until the peak stress (61.20 MPa). Upon applying the peak stress, there was a remarkable and unjustifiable jump of the strain to a comparatively high value. Then the expected gradual decrease of the strain was sustained henceforth throughout the un-loading session. The bad record at the data point becomes more obvious if one considers all the strains associated with the unloading stresses and those of their equivalent loading ones. The gap in the strain at this point compared to the preceeding and succeeding ones is so glaring and untypical of such measurement.

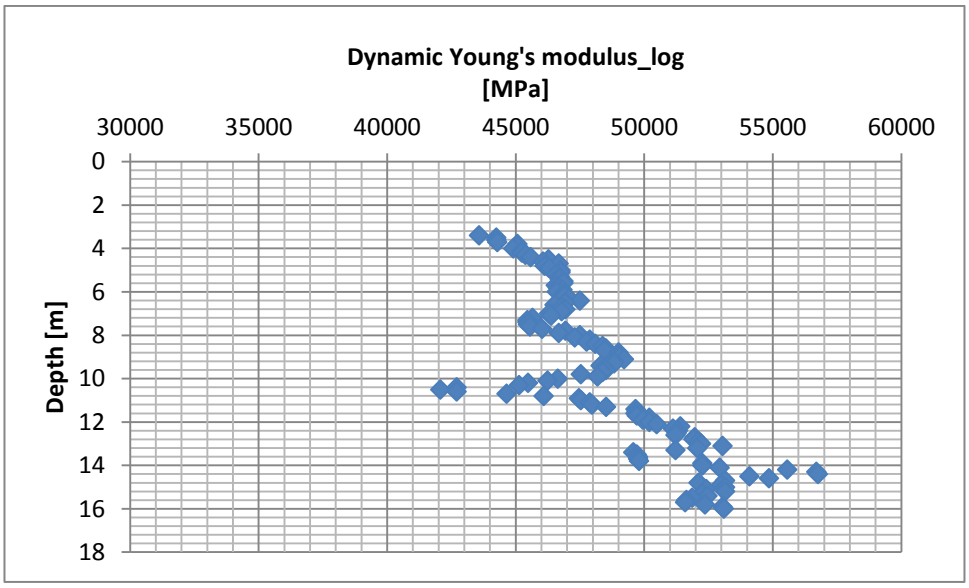

(a)

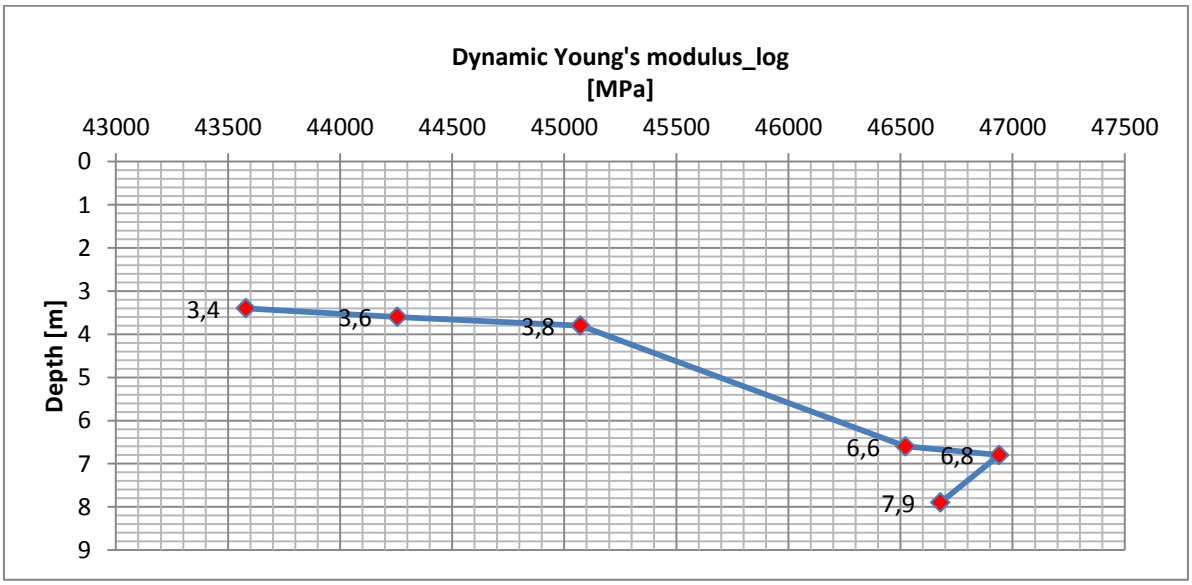

(b)

Figure 3.4: (a) Plot of calculated dynamic moduli against depths (BH 8). (b) A section of plot zoomed-in

Strains recorded during loading and unloading sessions at equivalent stress regimes are usually comparable (slight difference in values). A table for a similar measurement would be shown later and others could be found in the appendix for contrast with the current table. A possible explanation might be a failure of the sample at the peak stress without crumbling, which was most likely missed by the analyst.

It was decided therefore, that this highly inconsistent and possibly erroneous measurement for this sample depth be discarded, and use made of the available UCS value recorded for sample depth 14.1m in its stead. The hope is that whatever error using a UCS value together with values from a loading session might introduce, would not be as grievous as using the obvious bad measurement for sample depth 15.6m.

TM KB 09/13 15.60m						
Versuch durchgeführt am :			2015/06/11			
Lithologie:			Granitgneis			
					Programmauswertung	
Force [kN]	**Uniaxial Stress [MPa]**	**Height [mm]**	**Time [µs]**	**Strain**	**v_p [m/s]**	**v_s [m/s]**
5	0.61	196.99	73.42		-	-
10	1.22	196.69	-	0.00152	-	-
50	6.12	196.64	64.66	0.00178	3581.8	2085
100	12.24	196.58	62.92	0.00208	4005.3	2323
150	18.36	196.53	59.42	0.00234	4237.4	-
200	24.48	196.49	57.90	0.00254	4422.5	2472
500	61.20	194.17	49.67	0.01432	5112.4	-
200	24.47	194.24	53.66	0.01396	4644.7	2815
150	18.35	194.26	55.67	0.01386	4453.5	2709.3
100	12.24	194.28	58.93	0.01376	4246.6	2583.2
50	6.11	194.31	63.67	0.01360	3803.3	-

Table 3.1: Measured stress and strain values for sample core at 15.60m depth (BH 9)

The quality of data acquired for analysis of measurements from location 2 is abysmally poor. First, the sample names (IDs) of core plugs as recorded in the compressive test result (that is static moduli) could not match exactly those in the velocity (dynamic) laboratory result. And even when some similarity was established, the depth recorded for such similar samples vary in both results. Similarity was assumed for samples bearing the same digits (first three) in their ID, regardless of the associated varying alpha-numeric labels.

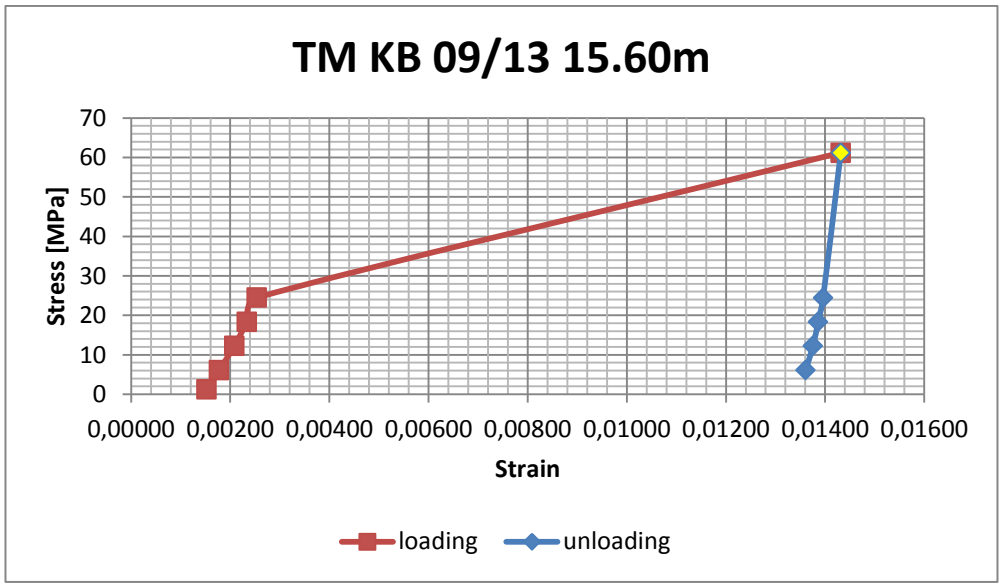

Figure 3.5: Stress-strain plot showing unusual loading and unloading sessions (15.60m depth, BH 9)

The alpha-numeric labels were assumed to be merely for indication of orientation or direction of coring within rock sequences. This was evidently a reckless assumption given that samples with the same numbering (but different alpha-numeric attachments) were recorded as being from different depths in the velocity-measured data. Also, the fact that the velocity (dynamic) laboratory measurement was carried out independent of the compressive laboratory (static) test, strongly suggested use of different core plugs (though, most likely from equivalent rock units) in both measurements. However, for lack of sufficient data for correlation despite the seemingly large repository, the assumption was sustained and the supposedly similar data used for analysis. The consequence of that was unusual results calculated for the parameters of interest. For instance, despite the widely conceived and proven fact that the laboratory dynamic (velocity) measurement is greater than the corresponding in-situ dynamic (log) measurement; the opposite was the case for all the rock types in this location (see table 3.6).

Further complication in understanding the underlying processes taking place in this location came from the granite-amphibolite rock interval. As can be seen in table 3.6, precisely at two different depths (3629.86m and 3709.32m) within this interval, the static values measured in the laboratory were higher than the dynamic values measured (separately) in the laboratory.

This made no sense. It is important to state that these two data values were among those that lacked matching sample IDs.

3.2 Standard correlations with raw data

Correlation of dynamic and static properties has evolved over the years. One of the oldest approaches, involved determination of the static values through laboratory compressive test and then correlating the values directly with in-situ dynamic values from log data. This was to be later considered unfair and biased given the different conditions (stress condition and apparatus) under which the properties being correlated were measured. With the advancement in ultrasonic velocity measurements, later investigations involved isolated measurements of both properties in the laboratory. The laboratory measured values could then be correlated first before applying relationship equation from such correlation to corresponding in-situ logs. This approach has also been improved upon by recent introduction of the so-called uniaxial and triaxial cells or units. Both units have the capacity to measure the dynamic and static properties simultaneously in one set-up. The triaxial unit being the latest, could additionally measure radial deformations, making it possible for 3-D strain investigations. It best simulates the actual in-situ stress-strain behaviours.

The choice of relationship type upon which correlations are based depend on available measured parameters and somtimes on some pre-conceived efficiency achievable by combination of measured parameters . While most static and dynamic properties analysis by authors who worked on igneous and metamorphic rocks seemed to be linearly correlated via linear regression; some others were correlated by using power law and logarithmic relationships. The later two, sometimes incorporates additional parameters as independent variables. In all the cases, satisfactory coefficients were recorded regardless.

For instance, one could consider power relationship if either or both properties varies as square or power values, and the logarithmic relationship for large volume of data or data with wide range (infinitesimally small and large numbers). None of these two considerations were adopted in this work. So, use was made of the more popular linear regression correlation.

Typical form of the equations for the relationship types are given below.

Linear regression ..... $E_{stat} = aE_{dyn} + b$ (e.g **King 1983**)

Power law ..... $E_{stat} = aE_{dyn}^{b}$ (e.g **Vanheerden 1987**)

Logarithmic ..... $Log_{10}E_{stat} = aLog_{10}(bE_{dyn}) + c$ (e.g **Eissa and Kazi 1988**)

The dependent and independent variables may change depending on properties being investigated, but these general forms usually do not change. Gegenhuber et al. (2017) applied the power law in their correlation of UCS against V_p .

3.2.1 Correlations for location 1

Estimation of static Young's modulus for any given location depend greatly on how representative the laboratory dynamic measurements are of the in-situ dynamic (log) measurements. It became imperative therefore, that the dynamic laboratory measurements be matched or compared with in-situ dynamic (log) measuremnts first before subsequent correlation with corresponding static laboratory data; and then the final projection of the static equation back unto the log data. This is important because many authors have proven that not only do these two dynamic measurements vary despite measurement method being the same, but also that the factors causing the variations do have great influence in the accuracy of the eventual static model equation. For instance, the value of the dynamic Young's modulus measured in the laboratory is proposed to be larger than the corresponding in-situ log measurement (Fjaer et al. 2008). The observed difference is in part due to differential stress conditions. The log measurements are affected by stress relief due to presence of fractures, microcracks and grain contacts or boundaries. This is not the case in laboratory measurements, where the cracks are closed-up under relatively higher pressure. Table 3.2 compares these values for equivalent depths. The correction for this assumed perfect compact composition of laboratory measurements would be addressed at a later section by the application of the simplified defect model calculation as proposed by Schön (2015). Other controlling factors include differences in frequencies of seismic wave propagation during in-situ logging and in the ultrasonic laboratory measurement.

And then possible anisotropic effects encountered during the borehole logging which might probably be insignificant in samples measured in the laboratory and vice versa.

Depth [m]	Dyn_lab [MPa]	Dyn_log [MPa]
Granite-gneiss		
2.3	54451.92	50712.90
3.4	57453.81	55117.40
3.6	57734.07	55350.97
3.8	57468.56	55705.28
White Schist		
6.6	55505.50	53211.14
6.8	54925.30	49522.92
7.9	49671.51	51040.98

Table 3.2: Calculated log and laboratory dynamic values for BH 10

Correcting for the later two factors involve some complex computations based on pore fluid measurements and precise knowledge of some velocity information for the samples. This is beyond the scope of this work. However, simple correlations would give an idea of how much these factors affected the results presented.

Dynamic data from the two measurement settings were crossplotted. The result show a very strong relationship and agreement for the granite-gneiss interval, with an outstanding regression coefficient of 0.98 (figure 3.6a). The white schist interval on the other hand, show very poor correlation of 0.04 for the two measurements (figure 3.6b).

Recall that the laboratory measurement value recorded at 7.9m depth, and also the log measurement at 6.8m depth both of which were within the white schist interval were highlighted as being erroneous in section 3.1. The next step was correlation of the dynamic laboratory measurements with corresponding static measurements. But before using the static data, it would be good to show how they were derived from the compressive test stress-strain curves. A more robust and popular approach called the tangent-modulus method was adopted. Other approaches include the secant-modulus method and the average-modulus method (see McCann and Entwisle 1992).

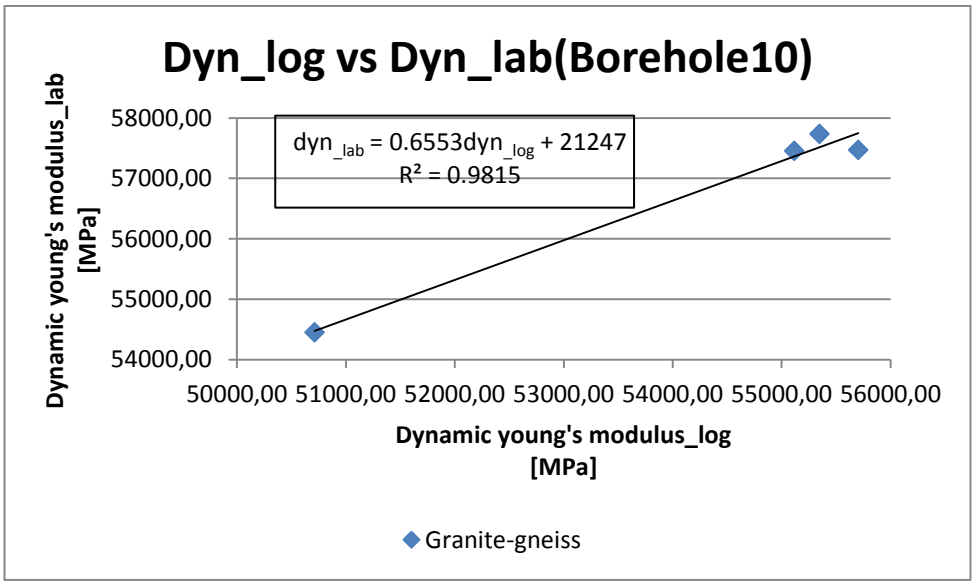

(a)

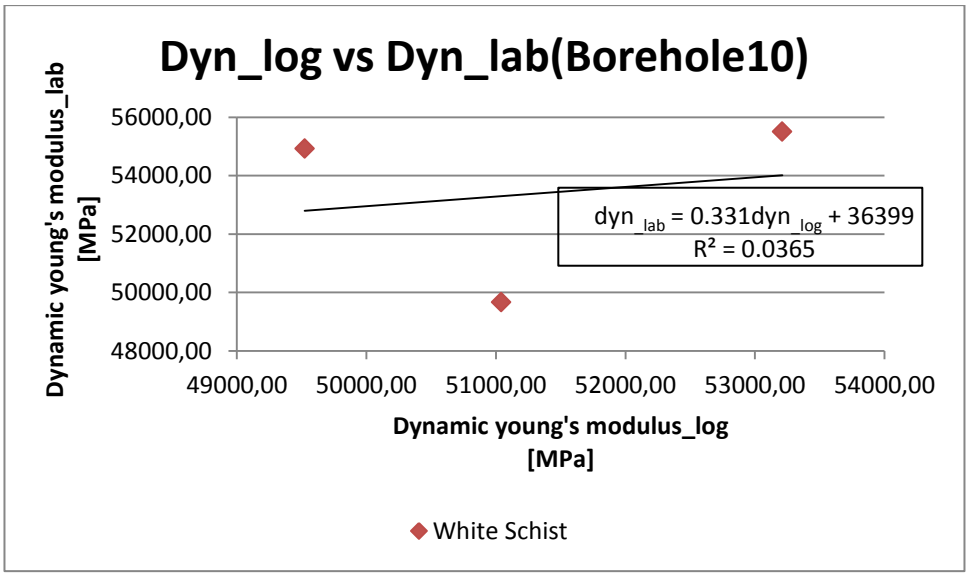

(b)

Figure 3.6: Log and laboratory dynamic moduli plots for (a) granite-gneiss. (b) white schist

The tangent-modulus method involves the calculation of the slope of the tangent to a plotted stress-strain curve, at a pre-determined percentage level of the ultimate stress (50% used for this work). Table 3.3 show the applied stresses with corresponding strains during loading (from 1.47 MPa to 61.31 MPa) and unloading (from 61.31 MPa to 1.23 MPa) sessions. Compare this table with table 3.1 to appreciate the error highlighted in section 3.1.

TM KB 10/13 2.30m						
Versuch durchgeführt am :			2015/06/11			
Lithologie:			Granitgneis			
					Programmauswertung	
Force [kN]	**Uniaxial Stress [MPa]**	**Height [mm]**	**Time [µs]**	**Strain**	**v_p [m/s]**	**v_s [m/s]**
12	1.47	204.90	86.40		-	-
50	6.14	204.81	72.12	0.00044	3307.7	-
100	12.26	204.72	66.36	0.00088	3676.7	2316.4
150	18.40	204.64	62.70	0.00127	3924.1	2436.2
200	24.53	204.58	60.81	0.00156	4098.2	2540.7
500	61.31	204.30	54.81	0.00293	4661.2	2932.8
200	24.52	204.52	60.06	0.00185	4172.2	2604.0
150	18.38	204.58	61.56	0.00156	3978.6	2466.3
100	12.26	204.65	64.08	0.00122	3823.8	2370.3
50	6.13	204.75	69.81	0.00073	3468.0	2109
10	1.23	204.87	80.82	0.00015	-	-

Table 3.3: Measured stress and strain values for sample core at 2.30m depth (BH 10)

Figure 3.7 is the stress-strain curves plotted using the values in table 3.3. The dashed green line marks the stress value corresponding to 50% of the ultimate stress before unloading, which is approximately 30.65 MPa. The convention is to use the curve for the loading session (red curve) for the calculation. So, the dashed green line was traced to the point of intersection with the red curve, and a tangent to the curve drawn at this point. The slope of this tangent was then calculated as the static Young's modulus for the depth indicated. Hence, from the given curve (at 2.3m depth) the slope or rather static Young's modulus was calculated thus;

$$Static\ Young's\ modulus = \frac{38 - 20}{0.0021 - 0.0014}$$

$$= \mathbf{25714.29\ MPa}$$

The calculated static values for the rest of the depth interval with their equivalent dynamic laboratory data is found in table 3.4. Also see the appendix for all the stress-strain tables and curves that produced the tabulated values.

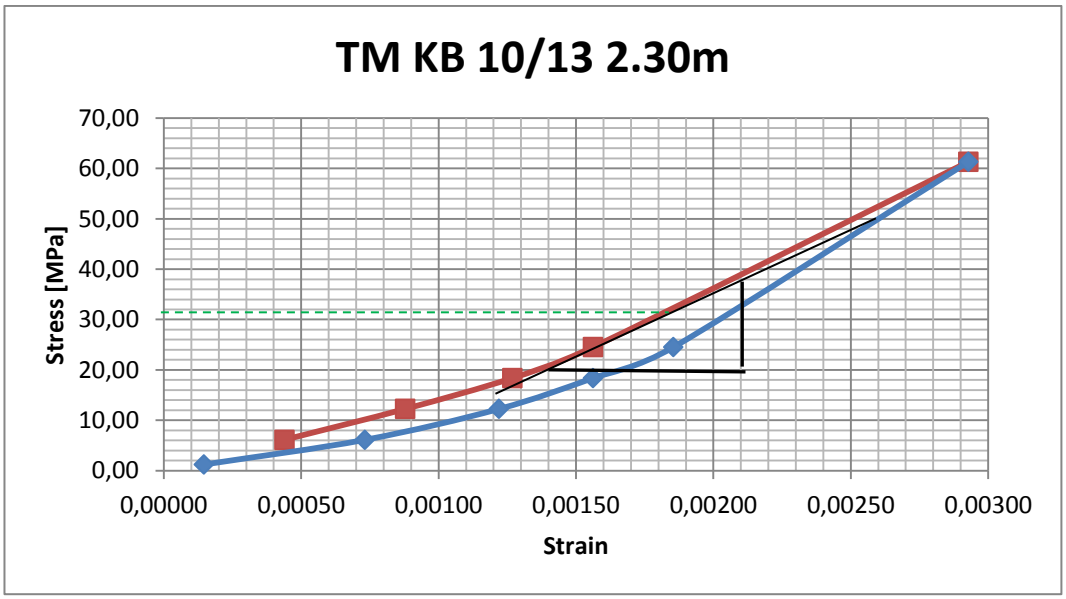

Figure 3.7: Stress-strain plot showing typical loading and unloading sessions (2.30m depth, BH 10)

Depth [m]	Dyn_lab [MPa]	Static [MPa]
Granite-gneiss		
2.3	54451.92	25714.29
3.4	57453.81	29230.77
3.6	57734.07	30000.00
3.8	57468.56	31666.67
White Schist		
6.6	55505.50	16153.85
6.8	54925.30	15714.29
7.9	49671.51	10000.00

Table 3.4: Calculated standard static and dynamic Young's moduli for BH 10

Figures 3.4a and 3.4b show the correlation of the laboratory static and dynamic moduli for the two rock types in borehole 10. Both correlations show strong relationships, with correlation coefficients of 0.82 and 0.999 for granite-gneiss and white schist respectively.

The near perfect relationship observed for this laboratory correlation with respect to the white schist is an indication that the poor dynamic correlation result discussed earlier were influenced more by errors from the log maesurements.

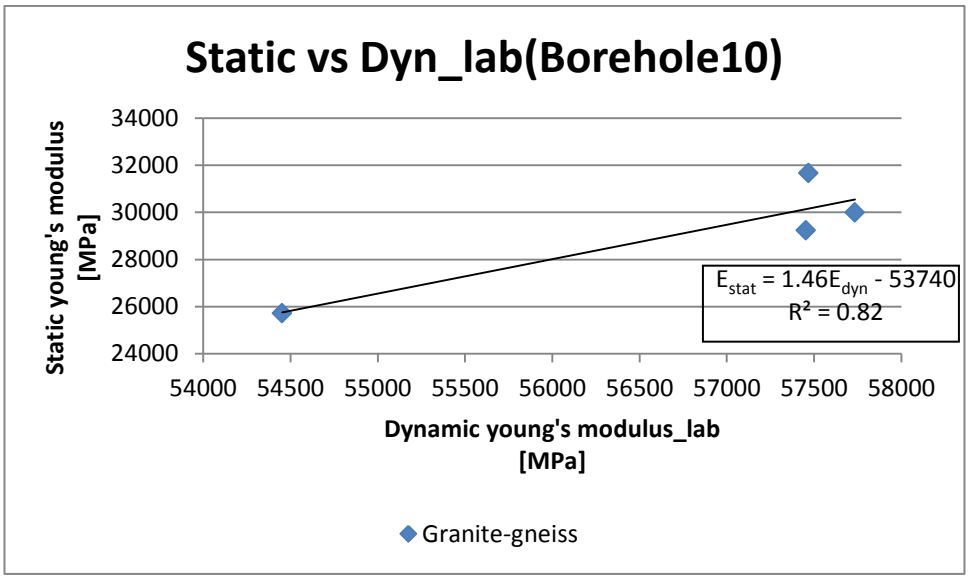

(a)

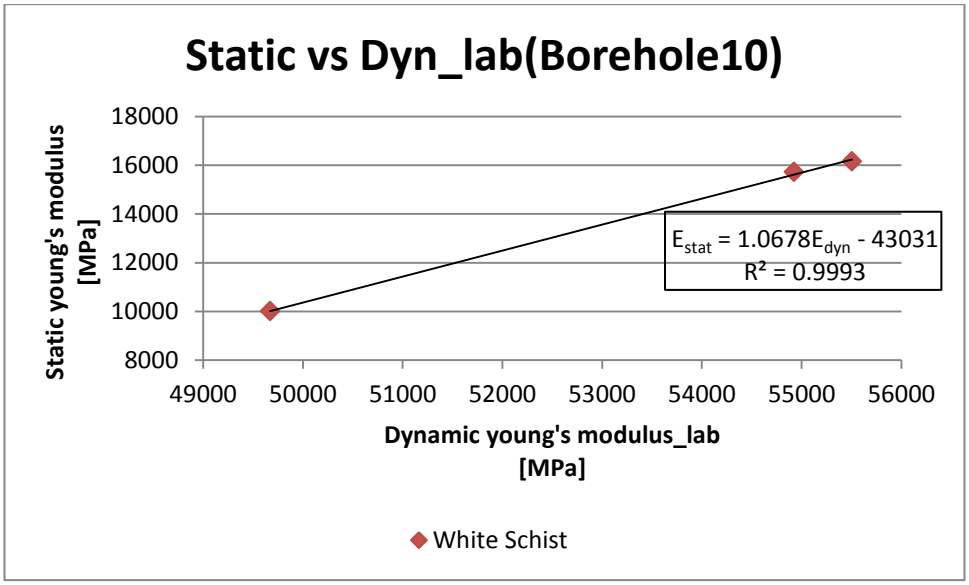

(b)

Figure 3.8: Standard static-dynamic regression plots for (a) granite-gneiss. (b) white schist

Standard correlation equations expressed in terms of the static Young's modulus (E_{stat}) for the granite-gneiss and white schist were given respectively in equations 2 and 3;

$$E_{stat} = 1.46E_{dyn} - 53740 \quad (R^2 = 0.82) \quad \text{..... (2)}$$

$$E_{stat} = 1.0678E_{dyn} - 43031 \quad (R^2 = 0.999) \quad \text{..... (3)}$$

The supposition here, is not only that these equations can be applied to the dynamic log measurements to estimate the in-situ static property in borehole 10, but can also yield reasonable estimates of the static property when applied to other boreholes in this location. However, it would be presumptous to apply them across the boreholes in the area without taking into account the effect of defects due to fractures. Hence the need for corrected model equations. This would be addressed in section 3.3.

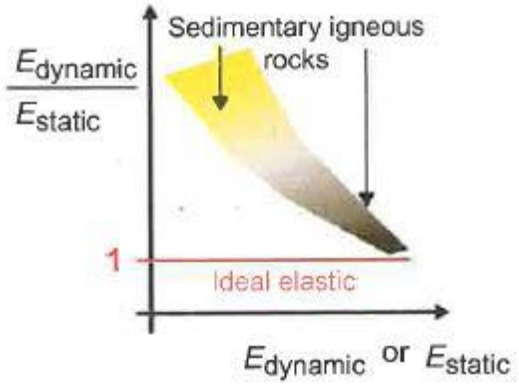

(Schön 2015)

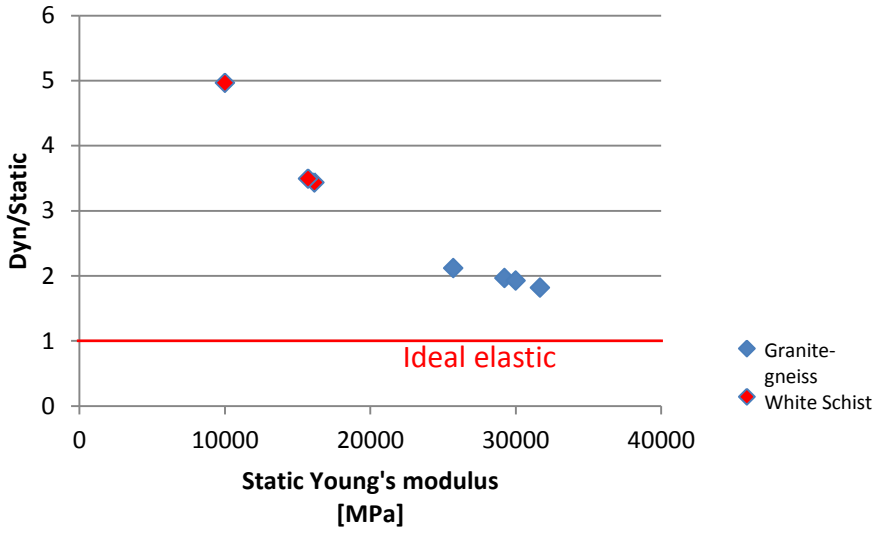

Figure 3.9: Plot of Dynamic-static ratio against static moduli, compared with model by Schön 2015 (top)

Schön (2015) suggested a plot of the dynamic/static ratios of various rock types with respect to their static properties as a good way to visualize their correlations.

He proposed a trend for the sedimentary and igneous rocks. Figure 3.9 compares the proposed trend and that established from current correlation. Evidently they matched, considering the sedimentary and igneous origin of white schist and granite-gneiss respectively.

As mentioned earlier, no laboratory measurement was carried out for Borehole 8. Borehole 9 on the other hand has laboratory measurements but lacked log measurements. Even the laboratory data has some missing velocity information, therefore the dynamic moduli could not be calculated. Therefore the plan was to use only the static moduli from its data and correlate the log data of boreholes 10 and 8 at equivalent depths. The established correlation equations from that could be used as alternatives for the granite-gneiss interval, especially in the estimation of static properties of the deeper section of borehole 10. The next task therefore, would be to analyse the laboratory data of borehole 9 and crossplot them with corresponding log data of borehole 10 and 8.

Depth [m]	**Static_well 9 [MPa]**	**Dyn_log-BH 10 [MPa]**	**Dyn_log-BH 8 [MPa]**
Granite-gneiss			
14.1	34700.00	59111.31	52942.34
15.4	30158.73	56217.20	52464.29
15.8	32786.89	59564.29	52368.92

Table 3.5: Calculated standard static (BH 9) and dynamic Young's moduli (BH 8 and BH 10)

Table 3.5 show the static moduli as calculated for borehole 9 and their corresponding log dynamic moduli from boreholes 10 and 8. See the appendix for the stress-strain tables and curves that produced the static values. Note that the value at 14.1m depth is a UCS value which was used to replace the bad static measurement for 15.6m depth (see section 3.1). The plot of their correlation is shown in figure 3.10a and figure 3.10b for boreholes 10 and 8 respectively.

The achieved regression coefficient of approximately 0.72 and 0.51 for the respective boreholes were reasonably good, considering that the properties were from different boreholes, not to mention the introduction of the UCS value. Hence, alternative set of correlation equations for the granite-gneiss rock type were obtained thus;

$$E_{stat} = 1.0651E_{dyn} - 29547 \quad (R^2 = 0.72) \quad \text{..... (4)}$$

$$E_{stat} = 5.3268E_{dyn} - 247600 \quad (R^2 = 0.51) \quad \text{..... (5)}$$

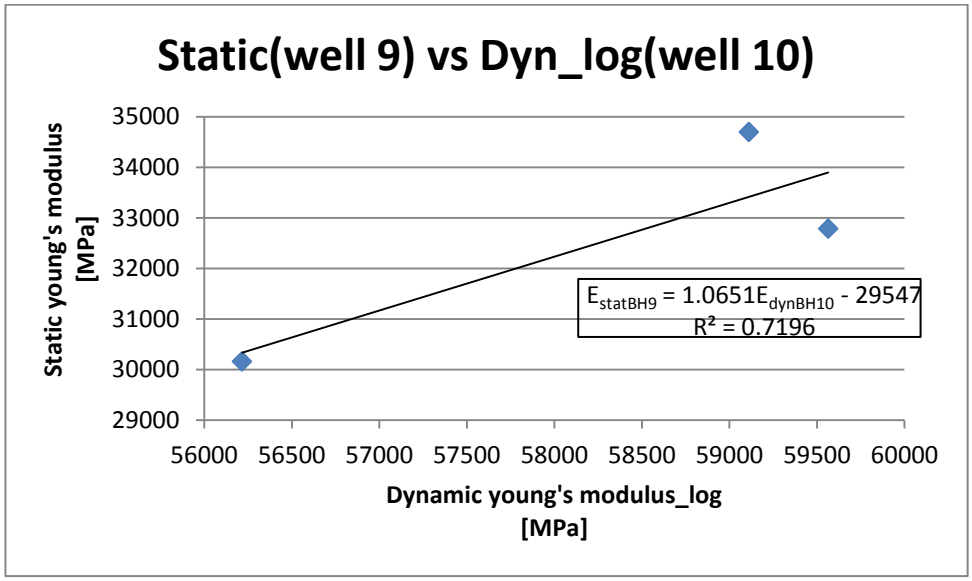

(a)

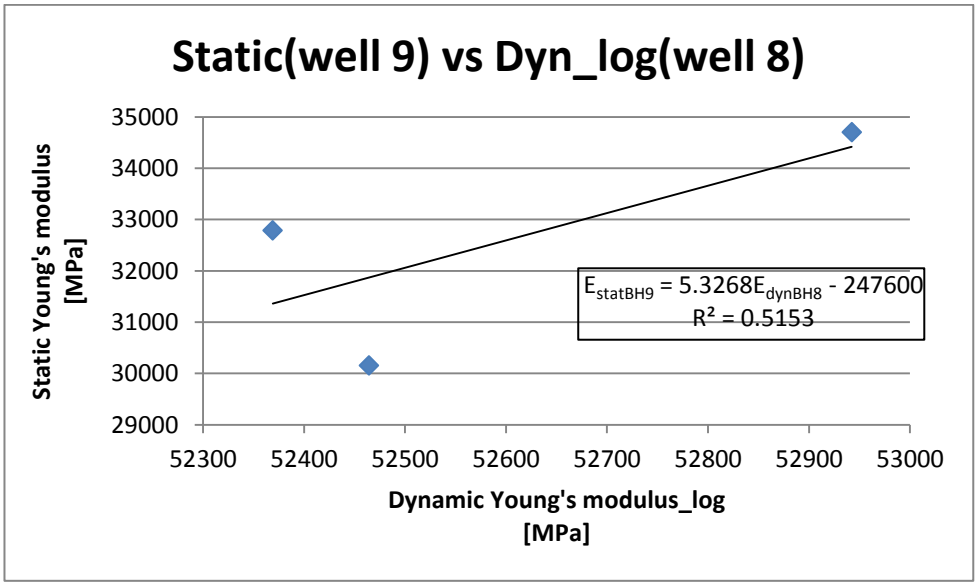

(b)

Figure 3.10: Regression plots using static data from BH 9 against dynamic log data from BH 8 and BH 10

3.2.2 Correlations for location 2

Table 3.6 show the measured laboratory static and dynamic properties in this location. Corresponding log dynamic values were added for comparison as done in section 3.2.1.

GNEISS(GNS)			
Depth [m]	**Static [MPa]**	**Dyn_lab [MPa]**	**Dyn_log [MPa]**
2355.54	47800	65170	89778
2444.85	59600	71506	73925
2466.06	27200	73671	89945
3538.85	43700	63152	76723
3558.34	57400	65104	74141
HORNBLENDE-GNEISS (HBL-GNS)			
2478.56	41100	58784	80918
2510.78	32700	71287	86475
2516.65	43900	83595	92925
2565.81	38800	68685	87979
GRANITE-AMPHIBOLE (GNT-AMP)			
3209.20	51700	82931	71638
3629.86	78800	75096	91787
3675.65	66200	93871	104380
3709.32	90000	76822	99628
3745.31	52300	85147	103899
BIOTITE-GNEISS (BIO-GNS)			
2612.65	45400	76196	83005
2632.14	26000	51592	77050
2698.27	25300	73158	76223
2715.10	9600	67203	73524
2824.27	19100	66492	62570
2841.70	5700	71856	75199
2866.07	10100	68530	71331
2948.96	22900	70298	74120
2983.10	29400	58341	80568
2997.95	33500	47127	75729
3011.29	42800	53078	73701
3032.32	14500	68532	74898
3104.35	44700	63749	73551
3133.20	49200	53233	74679
3146.99	36100	51311	70806
3185.98	46300	59590	69848
3196.24	20000	86908	81728
3243.35	25000	51473	70767
3422.49	18100	50890	76930
3436.70	33400	65005	77273
3460.54	32800	54140	77984
3480.93	33800	56611	81272
3498.30	36600	57427	80014

Table 3.6: Calculated standard static and dynamic Young's moduli for the Pilot borehole (location 2)

As discussed in section 3.1, data from this location were considered bad. The general trend of higher in-situ (log) dynamic values against the lower laboratory dynamic values is unusual, especially if one considers the extensive works of many authors proving the opposite. Added to that is the record of higher static values than dynamic values in the laboratory measurements of the granite-amphibolite interval (at two distinct depths). Yet, this interval appeared to be relatively more correlated in terms of measured properties. In fact, regression coefficient as high as 97.6% could be achieved if the two seemingly erroneous values are removed. But it was decided that the data would be used as they were because of the limited samples measured for this interval. The less the data used in a correlation, the greater the bias in applicability of its model result. Also, given what is known already about the data in this location, the objective ought not be the perfection of the correlation, otherwise one would fall for data fitting. A better approach would be to accomodate as many data as possible, test for the best model, and try as much as possible to make accurate and meaningful deductions from the model result. Figure 3.11 show the crossplots of the rock types traversed by the pilot borehole in this location.

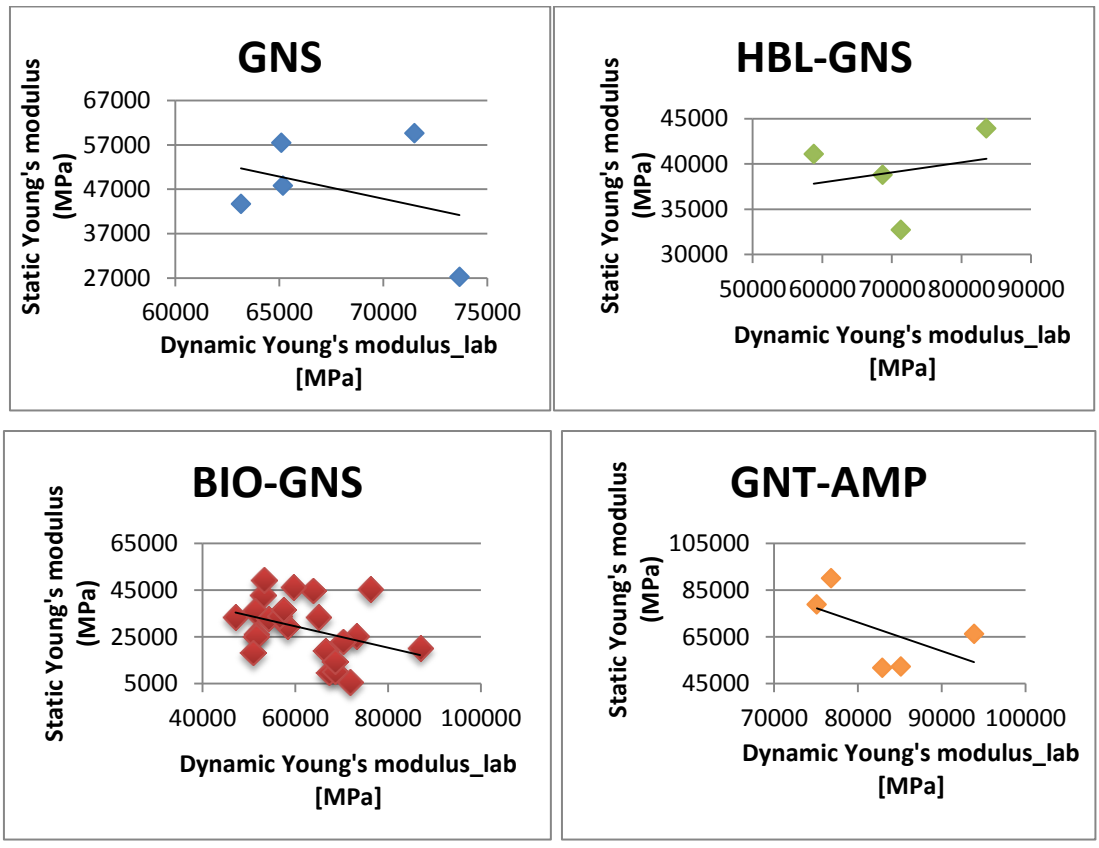

Figure 3.11: Regression plots for all rock types in the Pilot borehole at location 2

The correlations were expectedly poor for this borehole. However, the granite-amphibolite interval showed better correlation than the gneiss intervals. The static correlation equations and the corresponding regression coefficients for the rock types gneiss (GNS), hornblende-gneiss (HBL-GNS), granite-amphibolite (GNT-AMP) and biotite-gneiss (BIO-GNS) are given respectively below in equations 6,7,8 and 9;

$$E_{stat} = -1.0039E_{dyn} + 115127 \quad (R^2 = 0.13) \quad \text{..... (6)}$$

$$E_{stat} = 0.1117E_{dyn} + 31240 \quad (R^2 = 0.06) \quad \text{..... (7)}$$

$$E_{stat} = -1.2262E_{dyn} + 169294 \quad (R^2 = 0.30) \quad \text{..... (8)}$$

$$E_{stat} = -0.4586E_{dyn} + 57075 \quad (R^2 = 0.13) \quad \text{..... (9)}$$

Correlation of the gneiss intervals as one whole unit was considered. As stated earlier, correlation results are more meaningful and acceptable as representative of true state of measured quantities, if wider range or larger volume of data were used in the estimations. Figure 3.12 show similar correlation plot as before, but for the composites of the gneiss rock type considered as one unit.

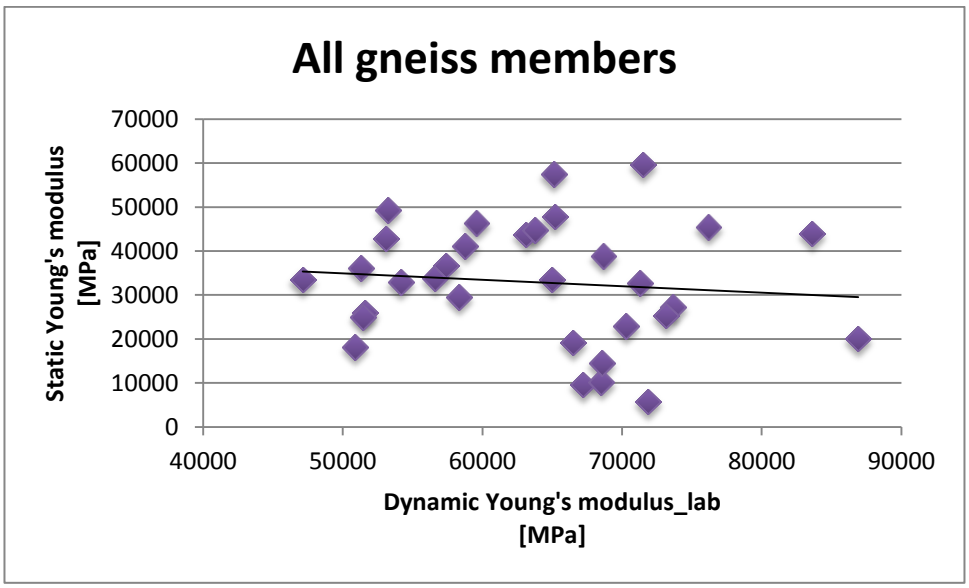

Figure 3.12: Regression plot for all the gneiss bearing intervals in the Pilot borehole

$$E_{stat} = -0.146E_{dyn} + 42213 \quad (R^2 = 0.01) \quad \text{..... (10)}$$

The combined plot suggests a negative relationship among the gneiss composites, which is similar to the trend shown by some of the individual intervals earlier. And the regression coefficient of 0.01 achieved, indicate extremely poor correlation (worse than what was achieved for the individual units). Nevertheless, the combined approach would be adopted in subsequent model calculations and further analysis.

3.3 Defect-model-based correlations

Fractures and microcracks undermines the accuracy in estimation of in-situ static properties. This is due to the closure of these in-situ features under pressure during laboratory measurements, and consequent recording of relatively higher values for the measured properties. In essence, in-situ static values are usually underestimated as their calculation is based on the bloated laboratory results. So, to ascertain if the samples contain significant fractures and microcracks, the measured data would be subjected to a model test as proposed by Schön (2015). The so-called *simplified defect model* compensates for closure of fractures and all similar defects in laboratory measurements, by ascribing a defect parameter. The defect parameter is assumed simply to be a cut in the relative depth or length of core samples but is taken to be representative enough of the complex geometries of fractures and other defects. There are quite a number of models addressing defects with respect to their varying shapes, sizes and fluid content. However, model calculations here are limited to the simplified defect model because its parameter definition and computation is relatively easy, and is adaptable to other detailed (shape-specific) models. The task in this section therefore, would be to exploit the relationship between the measured properties (measured velocities, computed dynamic moduli and measured static moduli) in establishing models with relatively wide applicability. Dynamic (laboratory) results were computed principally from laboratory measured velocities, so the relationship between them is quite evident. The model for static on the other hand, would be based on the widely conceived relationship between its measured values and the corresponding laboratory dynamic values. So, in compliance to Schoen's proposition, the equations needed for the defect model computations were formulated thus;

For dynamic laboratory measurements,

$$Dyn_{lab,model} = Dyn_{lab,solid} - Dyn_{lab,solid} * D$$

$$Dyn_{lab,model} = Dyn_{lab,solid}(1 - D) \quad \text{..... (a)}$$

$$V^2_{p,model} = V^2_{p,solid} - V^2_{p,solid} * D$$

$$V_{p,model} = V_{p,solid}(1 - D)^{0.5} \quad \text{..... (b)}$$

Substituting the value of (1-D) from (b) into (a) gave;

$$\boldsymbol{Dyn_{lab,model} = \left(\frac{Dyn_{lab,solid}}{V^2_{p,solid}}\right) * V^2_{p,model} = V^2_{p,model} * A_{dyn,V}} \quad \textbf{..... (11)}$$

In terms of the static laboratory (compressive test) measurements,

$$Stat_{lab,model} = Stat_{lab,solid}(1 - D) \quad \text{..... (c)}$$

Again, by substituting the value of (1-D) from (a) into (c) the model static property became;

$$\boldsymbol{Stat_{model} = \left(\frac{Dyn_{lab,model}}{Dyn_{lab,solid}}\right) * Stat_{lab,solid}} \quad \textbf{..... (12)}$$

where the parameters dubbed "solid" represent core properties measured in the laboratory, and assumed to be in defectless and compact state. Those with subscripts "model" represent the desired core properties as they would have been measured in the laboratory if their defected parts were not closed up. D is the defect parameter, while A is the matrix factor, and as could be seen from the equation is controlled by the solid or nonfractured matrix material properties.

Schoen also proposed that model properties derived from shear wave velocities give better correlations than those from primary wave velocities. He stated that this is because shear wave velocities (particularly for shallower or unconsolidated rocks) are controlled by skeleton properties of rocks. And these skeleton properties predominantly control the static mechanical properties. So, the next section would first compare calculations of "A" based on V_p and V_s respectively; and then proceed with the more robust velocity type to derive the model equations. The choice velocity type would also be adopted for the rest of the model calculations. Once more, note that $V_{p,model}$ or $V_{s,model}$ are equivalent to the FWS sonic log measured V_p and V_s respectively.

It would be presumptous to use one empirical in-situ velocity value for each of the rock types, given the large variation of their individual velocity records.

3.3.1 Derivation of model equations for location 1

By adopting the relationship in the middle of equation (11), the solid matrix factor "A" could be calculated as the slope in a linear plot of the dynamic laboratory property ($Dyn_{lab,solid}$) against the square of either the laboratory P or S wave velocities ($V^2_{p,solid}$ or $V^2_{s,solid}$). The linear equation was of the form y = ax, depicting exactly the relationship between the properties in the formular given in equation (11). Where **a** represents the slope, hence the solid matrix factor "A". And **x** represents the square velocity. Figures 3.13a and 3.13b are pairs of such plots based on V_p and V_s, for granite-gneiss and white schist rock types respectively. Confidence interval was determined for each of the data set at 95% , and the plots show good distribution of the core data within the intervals. This validates the calculated "A" values as being adequately representative of each rock type. It could also be seen from the plots that the calculations based on S-wave velocities were better. And the solid matrix factor seem to be the same in this case for both rock types. V_p would therefore, be replaced by V_s in the equations given earlier, for subsequent model calculations.

Using equation (11), values were computed for the model laboratory dynamic property ($Dyn_{lab,model}$). The same was done using equation (12) for the model laboratory static property ($Stat_{lab,model}$) (see Table 3.7). Figure 3.14 show plots of those model static and dynamic properties. The derived model equations are as given in equations (13) and (14) for the granite-gneiss and white schist intervals respectively. They could be compared with their equivalents from standard correlations done in section 3.2.1.

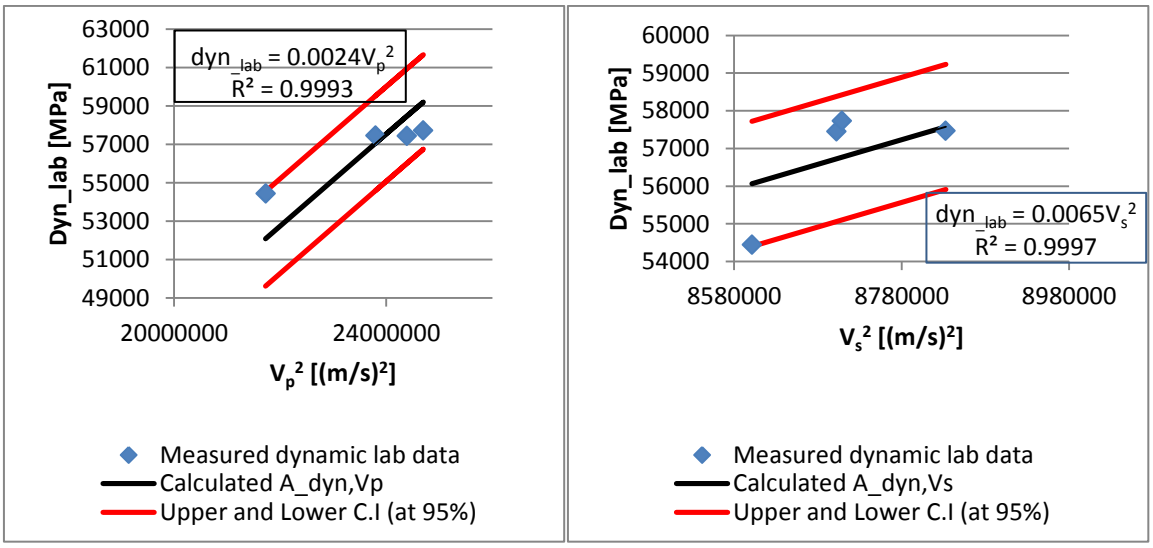

(a)

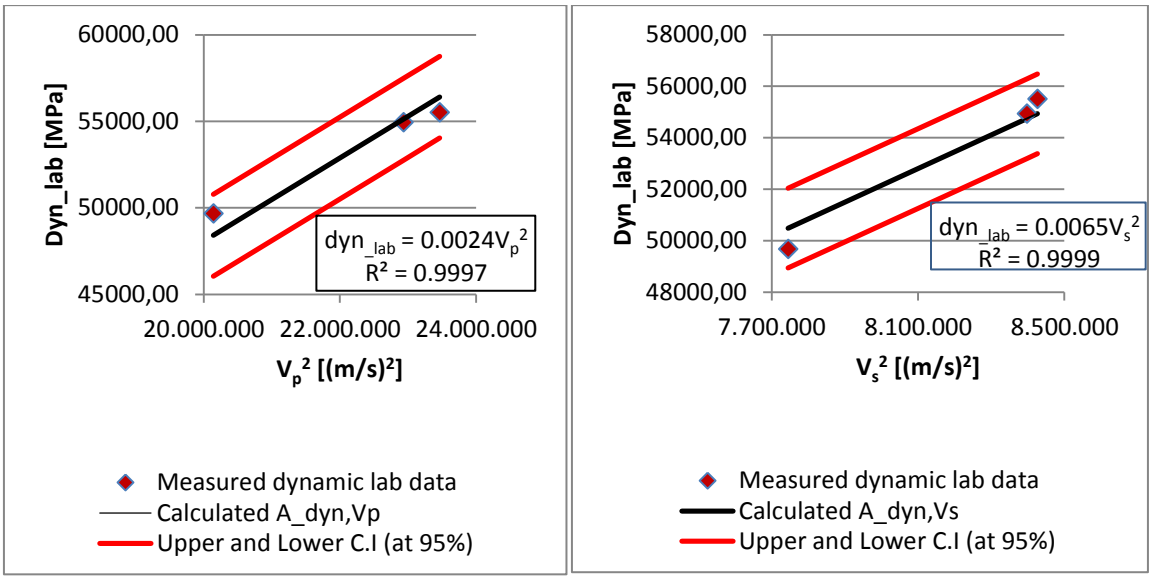

(b)

Figure 3.13: Calculated solid matrix factor (A) based on velocity type (a) for granite-gneiss (b) for white schist

The model equation derived for the granite-gneiss validated the defect concept. This could be seen in the form of an improvement in the regression coefficient from 0.82 recorded in the standard correlation to 0.91 currently recorded in the defect model correlation. The model however,failed in the case of the white schist.

The regression coefficient dropped from the near-perfect 0.999 in the standard correlation to 0.12 in current defect model correlation. This might be due to the introduction of the velocity component from log data in the model computation. Recall that it was established in section 3.1 that there was error in the log data for this rock interval.

Model calculations could not be carried out for borehole 9 for lack of sufficient laboratory velocity data (hence no laboratory dynamic property). Note that it's static data were earlier correlated directly with the log data of boreholes 8 and 10 respectively. Borehole 8 on the other hand has only log data for the granite-gneiss rock, therefore the model equation derived in this section for the same rock type, would only be applied to it's log data (see section 3.4).

A_{dyn},V_p	A_{dyn},V_s	V_{s_log} [m/s]	$Dyn_{lab,model}$ (based on Vs) [MPa]	$Static_{lab,model}$ [MPa]
Granite-gneiss				
0.0024	0.0065	2740.99	48834.67	132260.57
0.0024	0.0065	2857.54	53075.98	143747.44
0.0024	0.0065	2863.59	53300.96	144356.77
0.0024	0.0065	2872.74	53642.13	145280.76
White schist				
0.0023	0.0070	2807.69	55181.86	167944.80
0.0023	0.0070	2708.64	51357.11	156304.26
0.0023	0.0070	2749.84	52931.34	161095.38

Table 3.7: Calculated model dynamic and static properties with corresponding solid matrix factor (BH 10)

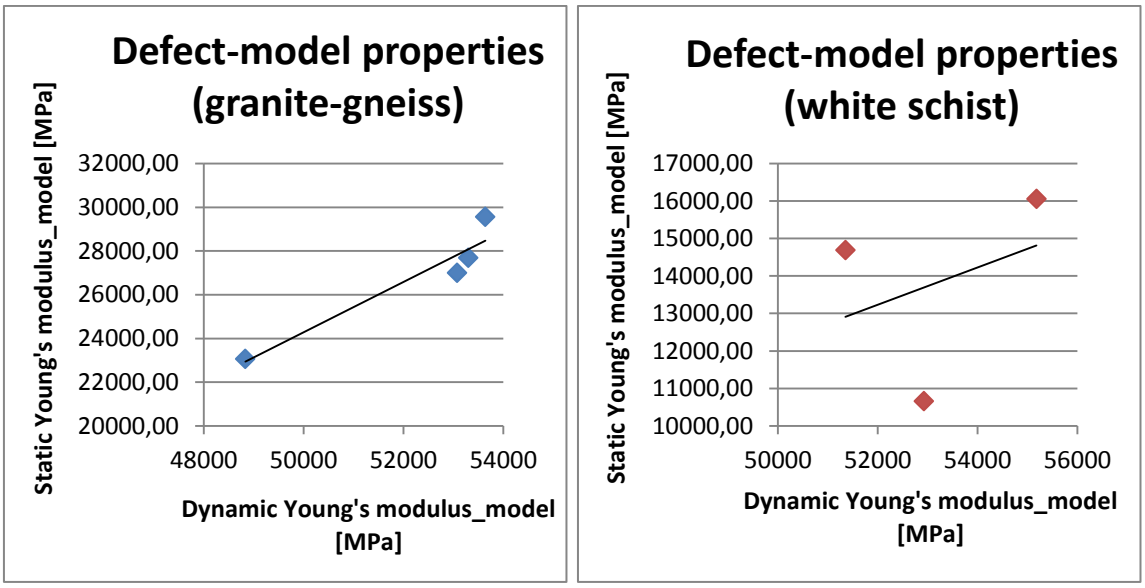

Figure 3.14: Defect-model regression plots for granite-gneiss and white schist respectively

$$E_{stat,model} = 1.152E_{dyn,model} - 33320 \quad (R^2 = 0.91) \quad \text{..... (13)}$$

$$E_{stat,model} = 0.4975E_{dyn,model} - 12643 \quad (R^2 = 0.12) \quad \text{..... (14)}$$

3.3.2 Derivation of model equations for location 2

Determination of the solid matrix factor for the two major rock types (gneiss intervals and granite-amphibolite interval) encountered in this location preceded the model calculations. Figures 3.15a and 3.15b show the plots of the solid state dynamic and shear wave velocity measurements for those major rock intervals respectively. The solid matrix factor of 0.0067 recorded for the gneiss intervals here, is reasonably close to 0.0065 obtained for granite-gneiss in location 1. This implies a somewhat consistent skeleton property for gneiss rock type in both locations despite the difference in associated mineralogical constituents.

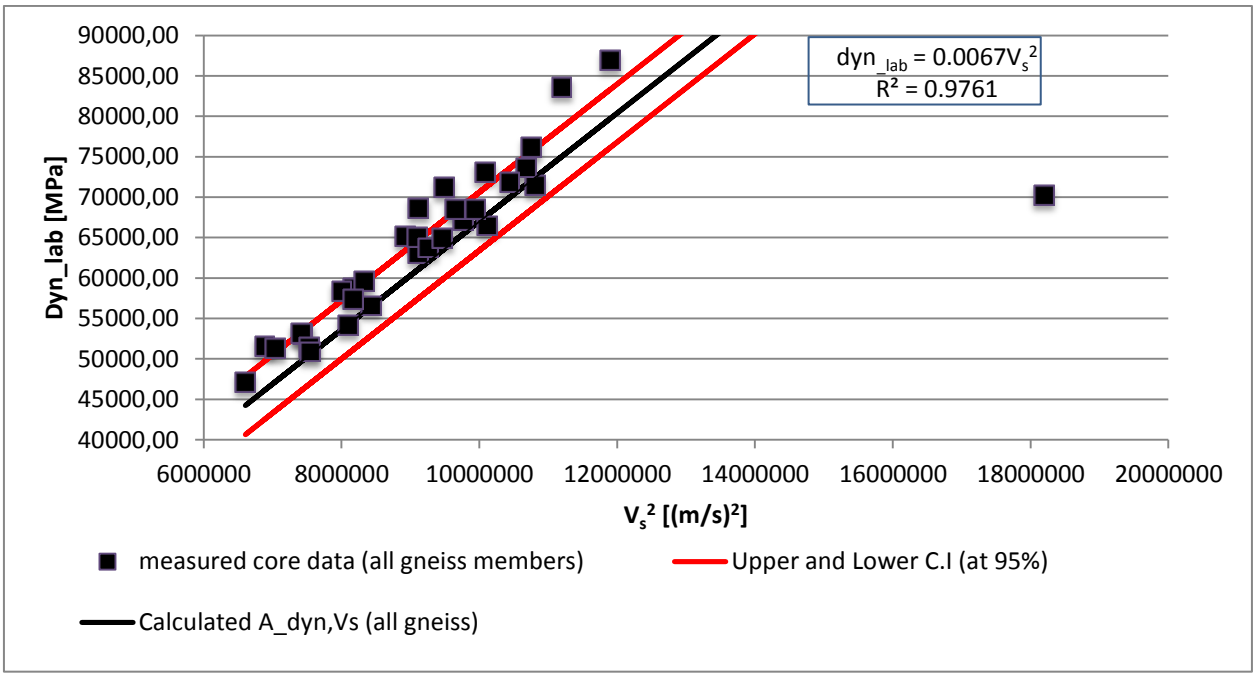

(a)

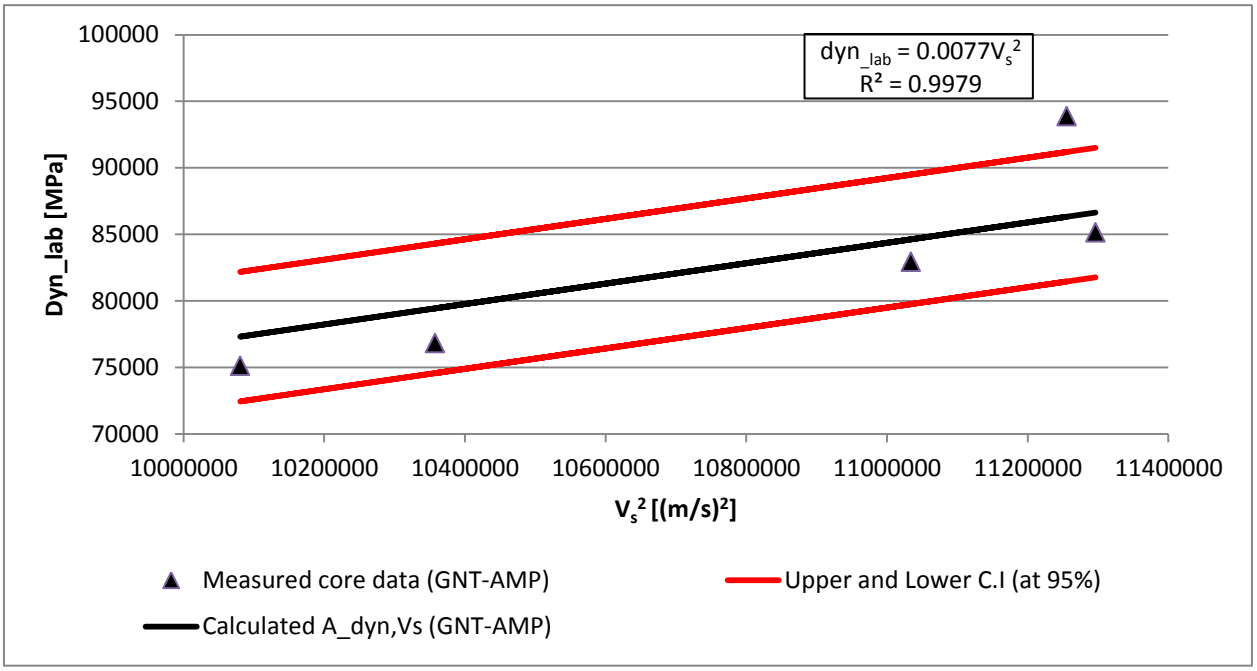

(b)

Figure 3.15: Calculated solid matrix factor (A) based on V_s (a) for all gneiss intervals in the pilot borehole (b) for granite-amphibolite

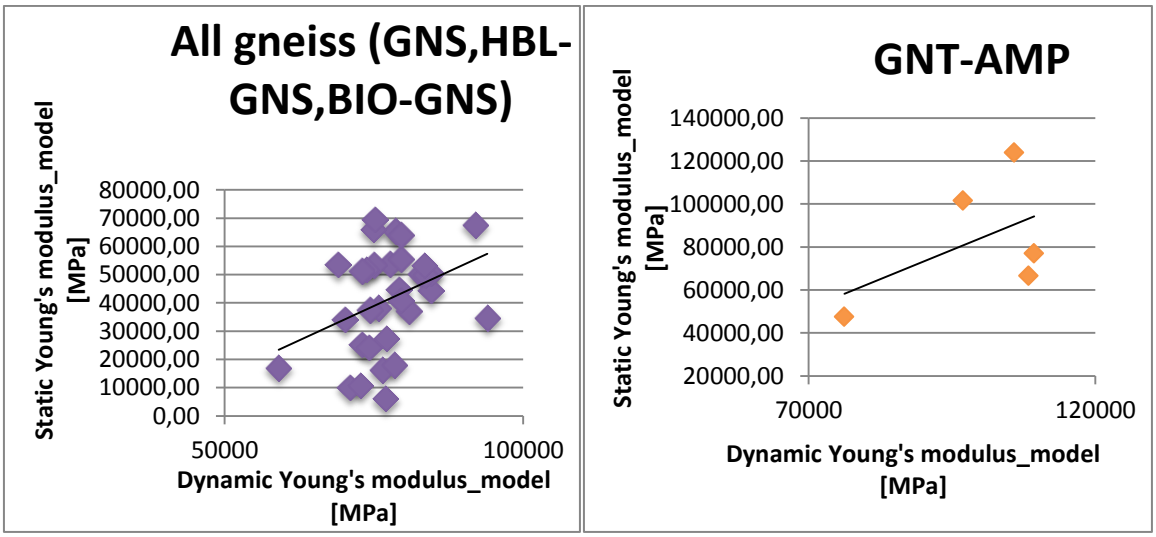

Figure 3.16: Defect-model regression plots for the combined gneiss intervals and granite-amphibolite respectively

Model dynamic and static properties were computed for all the gneiss intervals as a unit, based on the calculated common "A" value of 0.0067. The same was done for the granite-amphibolite interval based on the obtained value of 0.0077. Figure 3.16 show plots of model properties for both major rock groups. Model correlation equations derived from the plots are given below.

$$E_{stat,model} = 0.9697E_{dyn,model} - 33826 \quad (R^2 = 0.12) \quad \text{..... (15)}$$

$$E_{stat,model} = 1.0912E_{dyn,model} - 25016 \quad (R^2 = 0.25) \quad \text{..... (16)}$$

For the gneiss members, the model result show a ten-fold increase in their correlation; from a regression coefficient of 0.01 obtained in standard correlation to the current 0.12. Also, the model result produced a positive relationship as against the negative observed in the standard correlation. This implies that the defect model was successful here. However, it is evidently not good enough to be adopted for in-situ estimation of static properties in the entire location. The poor model result might be due to errors and inconsistencies caused by poor quality of raw data as explained in section 3.1. It is expected that certain minimum level of defects should cut across rock units in a borehole.

Thus, the simplified defect model should at least correct or compensate for these minimum level defects. And this is usually recorded in the form of slight improvement in existing low or high correlation between properties (not necessarily the enforcement of some high level of correlation). So, once again the model passed for the gneiss intervals but was not good enough to be representative. For the granite-amphibolite however, it failed. Model result of this rock interval show a drop in the regression coefficient from 0.30 calculated in the standard correlation to 0.25 in the current model computation. The result suggests that the supposed closure of defects in core samples, as formulated in the model never happened. Interpreting this development could be complicated, moreso given the observed unusual trend of the raw data. Recall that the laboratory measured dynamic values were found to be less than the corresponding log (in-situ) dynamic values. Also, some of the static values obtained from the laboratory compressive tests were larger than the dynamic values measured (independently though) in the laboratory. These abnormalities also discussed in section 3.1, could account for the failure of the model for this rock type.

3.4 Application of derived model equations to log data

Dynamic values computed from in-situ velocity log data were inserted as the dynamic parameter in the model equations. This was done to generate calibrated model values that represent the in-situ static property. Static values thus generated, were plotted in log traces comparable to traces of the dynamic log data and also traces of static estimates from standard correlations. The Wellcad software was used for this visual analysis. Also, inclusion of the core (raw) static data in the plots made it easier to visualize and analyse the fitting of the models. Figure 3.17 show log traces for the granite-gneiss rock unit in borehole 10. Clearly, static property from both standard and model correlations mirror the trend of the dynamic log data. The model static were better though, and showed very good fitting with the core data. This further confirms the model to be good, and validates the correlation level established earlier for this rock interval.. Note that the same scale was chosen for all the traces for ease of comparison. It could also be seen that the static moduli computed with standard correlation method are lower than those of the model correlation.

Log section for the white schist show different trend from the granite-gneiss, but do however, reflect the same results as observed in its correlation plots earlier (figure 3.18).

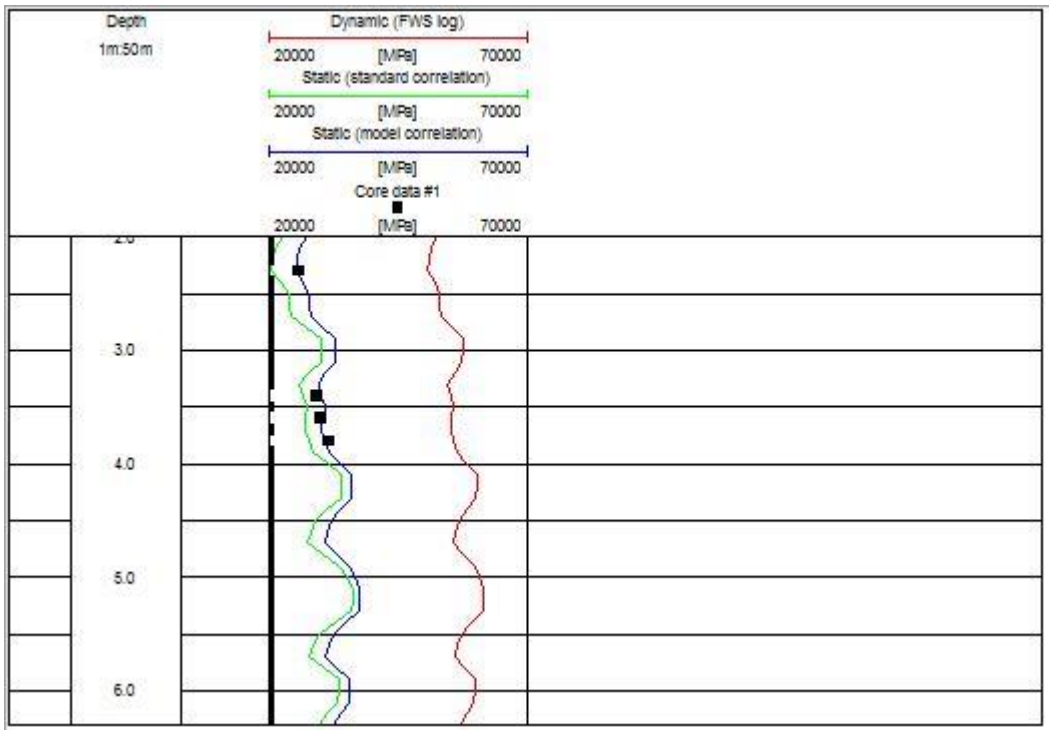

Figure 3.17: Log section comparing model result with dynamic log data (granite-gneiss)

In its section, the trace for standard correlation show a much better match with the dynamic log data than that of the model correlation. Recall that the model correlation did fail for this rock unit. So, the image reasonably depicted that observed correlation result. However, note that despite the agreement of standard correlation with log data here, the core data did not fit its trace with the same precision as would be expected given its near-perfect regression coefficient obtained earlier.

Applying the same model equation for the granite-gneiss (borehole 10) to the dynamic log data of borehole 8 produced the log section displayed in figure 3.19. This was done for lack of laboratory data for this borehole. The result would actually serve dual purpose.

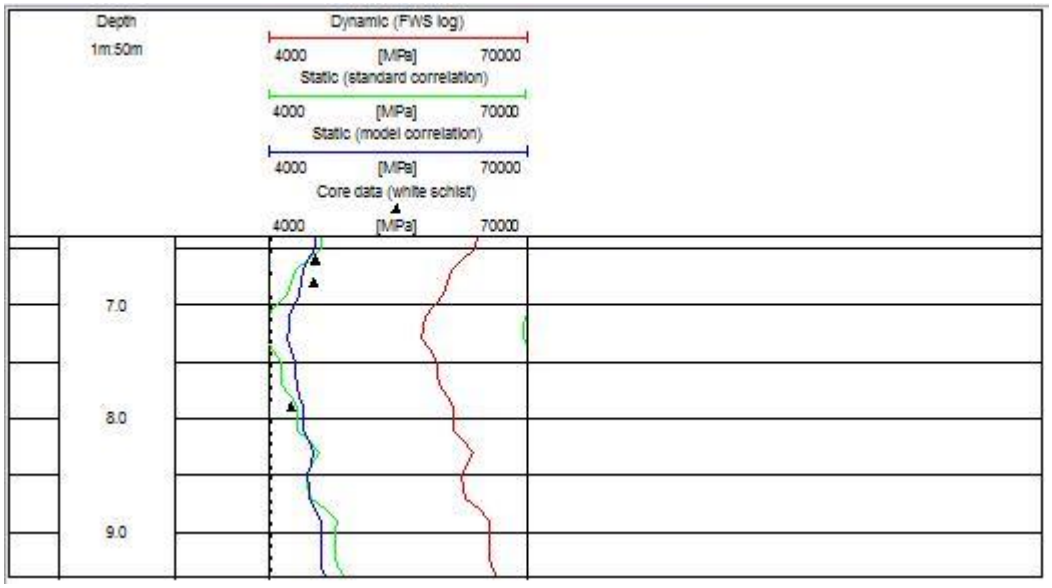

Figure 3.18: Log section comparing model result with dynamic log data (white schist)

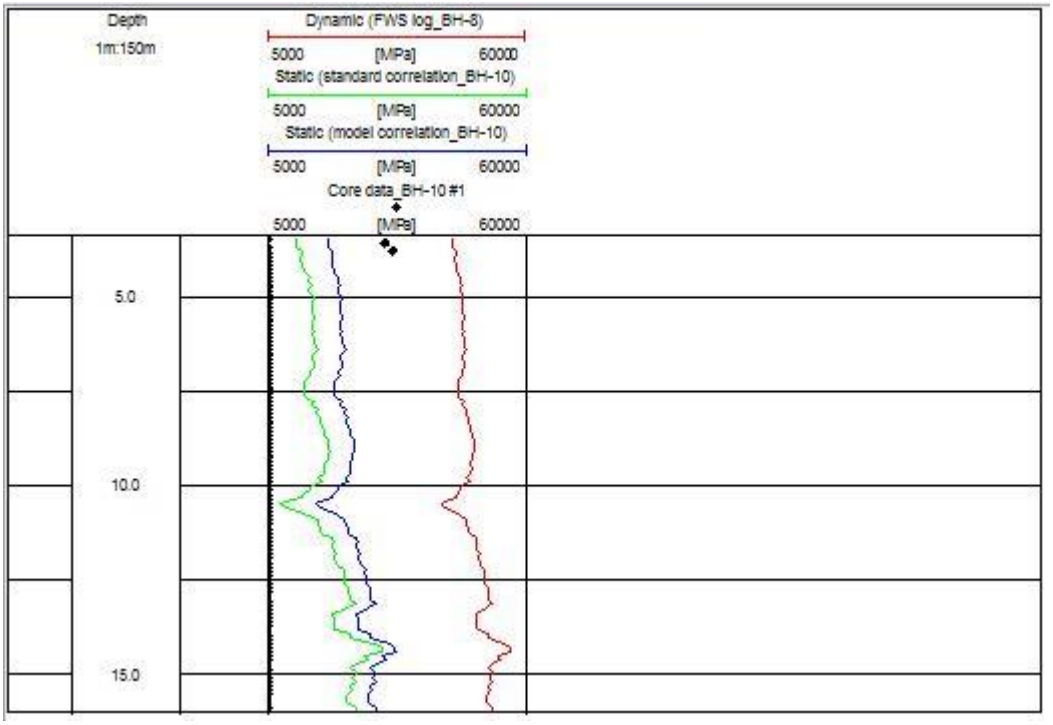

Figure 3.19: Log section comparing model result (BH 10) with dynamic log data of BH 8

First it would be a means of estimating in-situ static Young's moduli for borehole 8. And then, it would serve as a test for location-wide applicability of the model equation derived for the granite-gneiss rock type. Traces of both standard and model correlation approaches show good match with the dynamic log data in this borehole. The core data however, did not fit any of the traces. Understandably they don't have to, because they were sourced from a different borehole (BH 10). Therefore, the model is considered good nevertheless, for this borehole.

Application of model equations in location 2 was limited to depth range where core samples were collected, due to the large volume of log data available. Considerations within the range however, were carried out at reasonably small and consistent intervals so as not to miss any layer that might be of interest, and at the same time not to over-analyse a particular section. For the range comprising of the composite gneiss rock types, application interval of 25m from 2325m depth to 3575m was chosen. And for the shorter range granite-amphibolite rock unit, a smaller interval of 5m was chosen covering depths 3630m to 3750m.

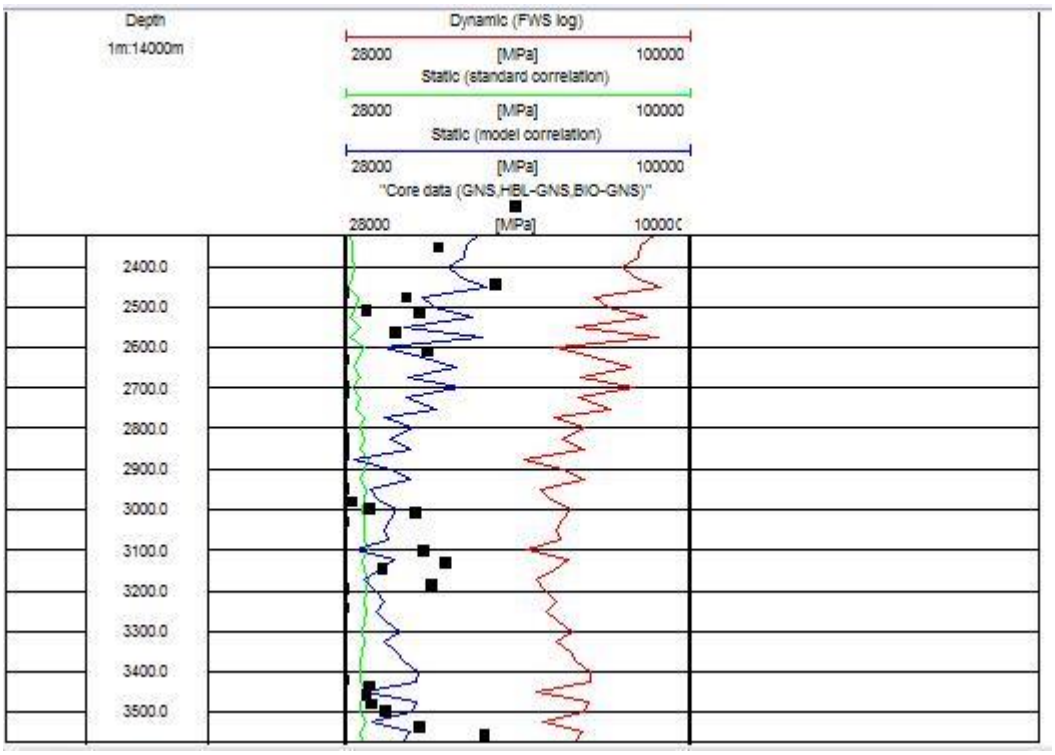

Figure 3.20: Log section comparing model result with dynamic log data

(combined gneiss intervals at location 2)

Figure 3.20 show comparable traces of model, standard and dynamic log traces for the combined gneiss units in this location. The model trace show relatively good match with the dynamic log data, but the fitting with core data was quite poor. The trace for standard correlation did not match the dynamic log data nor did it fit with the core data. This is in complete agreement with correlation results discussed previously for this rock type; where the regression coefficient for the standard correlation was much lower than that of the model correlation. The section for the granite-amphibolite on the other hand, show bizarre trace combination. The trace for standard correlation was reversed in polarity compared to the dynamic log and the model traces (figure 3.21)

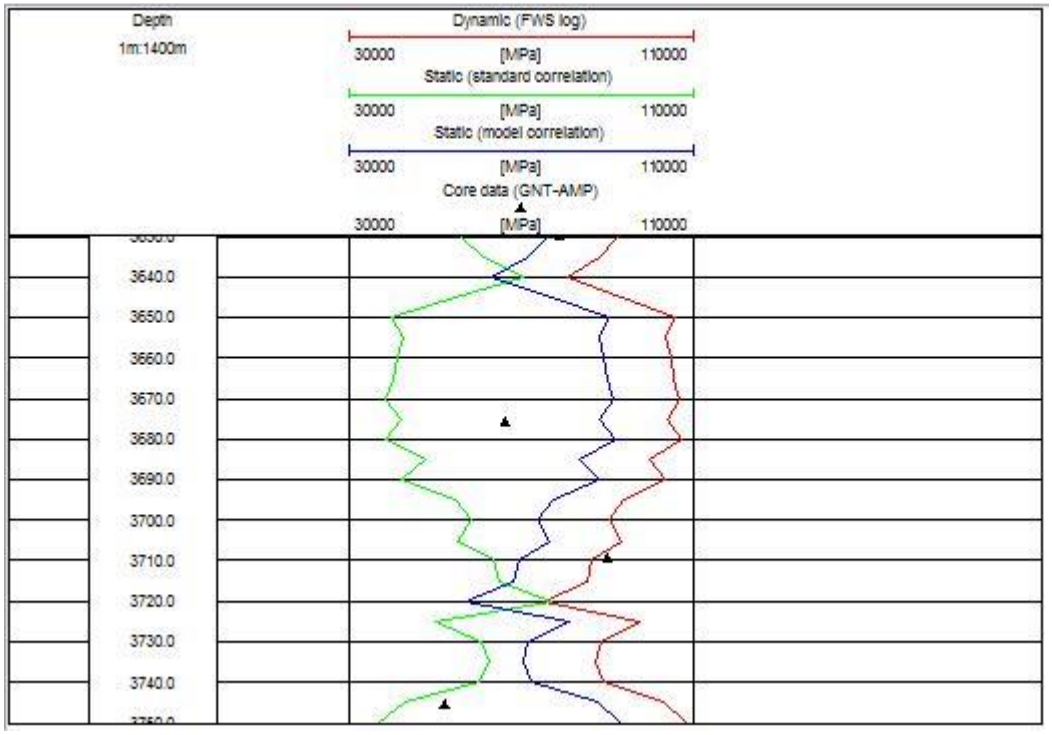

Figure 3.21: Log section comparing model result with dynamic log data (granite-amphibolite)

Also, the model trace seemed to match the log data, except for the lack of good fit with core data. This does not support the failure of the model as established in the previous correlation plots for this rock type.

3.5 Comparison of model results with literature

The type of rock samples investigated was particularly considered in deciding which of the many correlation equations available in literature to be used to compare current model equations. As could be observed, rock samples for the current study were all from metamorphosed formations. So, the objective was to apply only correlation equations of authors whose sample were or included cores of metamorphic origin; and also those who claim that their equation could be adopted for all rock types. In compliance to this requirement, published models of four authors were considered adequate for this comparison. Christaras et al. (1994) compared the dynamic elastic moduli computed from ultrasonic velocity and resonance frequency for different rock types with the corresponding static elastic moduli. They recorded a regression coefficient of 0.99, and proposed a model equation that would supposedly work for all rock types. Similarly, King (1983) investigated correlations between these elastic properties for a range of igneous and metamorphic rocks from the Canadian shield. He achieved a 0.82 regression coefficient. Eissa and Kazi (1988) proposed a model with regression coefficient of 0.70, and claimed it is suitable for all rock types. Starzec (1999) investigated the same relationship for a set of igneous and metamorphic rocks from Sweden, and came up with regression coefficient of 0.82 for the rock types. Table 3.8 show the model equations of these researchers as well as those from current work, the corresponding regression coefficients and the range of values of the dynamic moduli for which the equations are valid.

By applying the equations in table 3.8 to the dynamic log data in current work, log traces as well as regression graphs were plotted in order to compare the different models. For an unbiased assessment, a maximum limit was set within which the models could fairly be compared and beyond which a model is considered unrealistic or core data considered highly erroneous. Ideally, the predicted static moduli is supposed to be equal to the in-situ dynamic moduli in every measurement and for all locations. But for reasons already discussed in previous sections, this is not the case in real field measurements. In fact, no published work ever showed them to be equal. Calculations based on this known principle provided the upper boundary for the model comparisons.

Source	Model equation	Regression coefficient	Rock type	Valid range of Dynamic moduli [GPa]
King (1983)	$E_{stat} = 1.263E_{dyn} - 29.5$	0.820	Igneous & Metamorphic	40 - 120
Eissa and Kazi (1988)	$E_{stat} = 0.74E_{dyn} - 0.82$	0.700	All rock types	5 - 130
Christaras et al. (1994)	$E_{stat} = 1.05E_{dyn} - 3.16$	0.990	All rock types	25 - 110
Starzec (1999)	$E_{stat} = 0.48E_{dyn} - 3.26$	0.820	Igneous & Metamorphic	10 - 125
Model Correlation (location 1)	$E_{stat} = 1.152E_{dyn} - 33.32$	0.910	Metamorphic (granite-gneiss)	40 - 60
	$E_{stat} = 0.4975E_{dyn} - 12.64$	0.116	Metamorphic (white schist)	50 - 60
Model Correlation (location 2)	$E_{stat} = 0.9697E_{dyn} - 33.83$	0.123	Metamorphic (all composite gneiss)	50 - 100
	$E_{stat} = 1.0912E_{dyn} - 25.02$	0.253	Metamorphic (granite-amphibolite)	70 - 120

Table 3.8: Current and classic model static equations applied to dynamic log data (modified from Brotons et al. 2016)

So, consider the ratio of the dynamic moduli to the static moduli (k) for instance, and for all data. Assuming both properties to be equal implies k=1. Figure 3.22(top) show a plot of such ideal or theoretical k values (black line). Model plots below this line comply with the real expectation of k being greater than 1 (higher dynamic moduli). While plots above the line would indicate k values less than 1 (higher static moduli), which would mean bad model. Another complimentary measure for comparison is the fitness of models to the measured core data. Regression line of best fit (red line) based on core data, provided good means of comparing model closeness to measured core data. A good and acceptable model therefore, should match the dynamic log data in the log traces and also reasonably fit the measured core data in both the log and in the regression plot.

The log traces (figure 3.22 (down)) and the regression plot (figure 3.22(top)) for the granite-gneiss both agree in established fitness of the classical models and the current model, to the dynamic log data and the measured core data. One instance of such agreement is the approximate coincidence of Christaras' model static trace with the dynamic log trace, and then it's coincidence with the ideal k line in the regression plot.

His model therefore, represents the ideal situation explained earlier; and seem to propose static values approximately equal to the dynamic values for that rock type. Given the extensive research works in this subject, this is not a good model for this rock type and location, as equality of the two properties has never been recorded. It was obvious therefore, that it overestimates the static propeties for this rock type. Starzec's model on the other hand proposes static values lower than the measured core data. However,his model is the next closest in fitting to the measured core data after the current model. King's model with Eissa and Kazi's model showed points of common static estimates, and are considered neither bad nor best. The best model seemed to be the current model. Its good fit as observed in both figures justified its high correlation result established earlier for the granite-gneiss rock type. Note that though Starzec's model suggested low static values in this case, it is more acceptable than the other classic models because underestimation of static properties, though not usually desired, is much safer in engineering designs and constructions than overestimation. Figure 3.23 show similar comparisons for the white schist rock interval. One could see Christaras' model once again predicting static values that are roughly equal to the dynamic log values. Starzec's model predicted static values higher than the measured core data this time, but hardly matched the dynamic log data in terms of log traces. The current model fitted perfectly with the measured core data in the regression plot, but the fitting was not repeated in the log section. It also showed poor match with the dynamic log data in terms of the traces. Therefore, the current model and Starzec's model despite suggesting low values close to the measured core data in the regression plot, was not good for lack of the same level of fitting in the log section. Again, this justified the failed model result as established in previous correlation. The best model for this rock interval seemed to be King's model, followed by Eissa and Kazi's model.

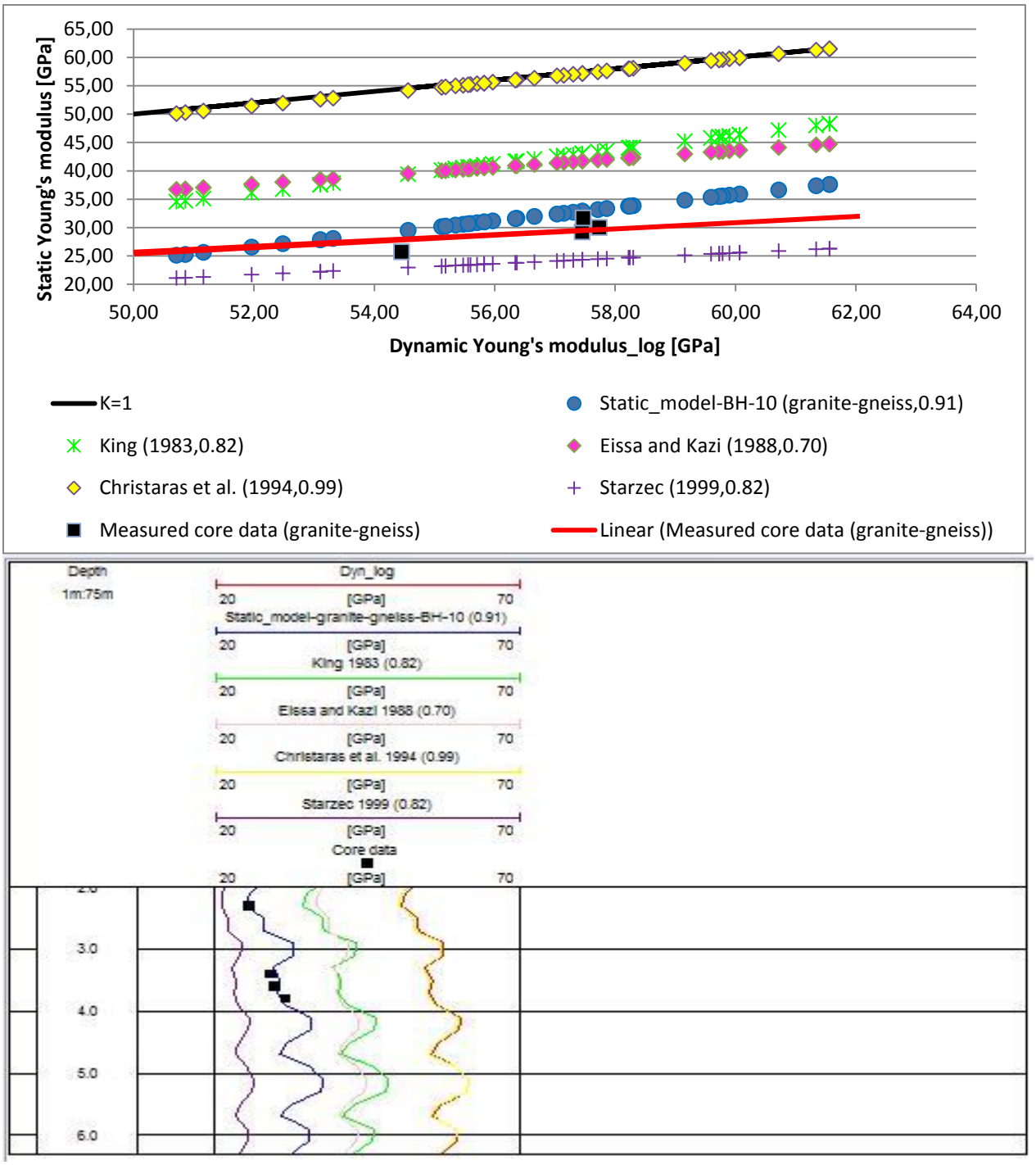

Figure 3.22: Comparison of current model with classic models for granite-gneiss using regression plot (top) and log section (bottom)

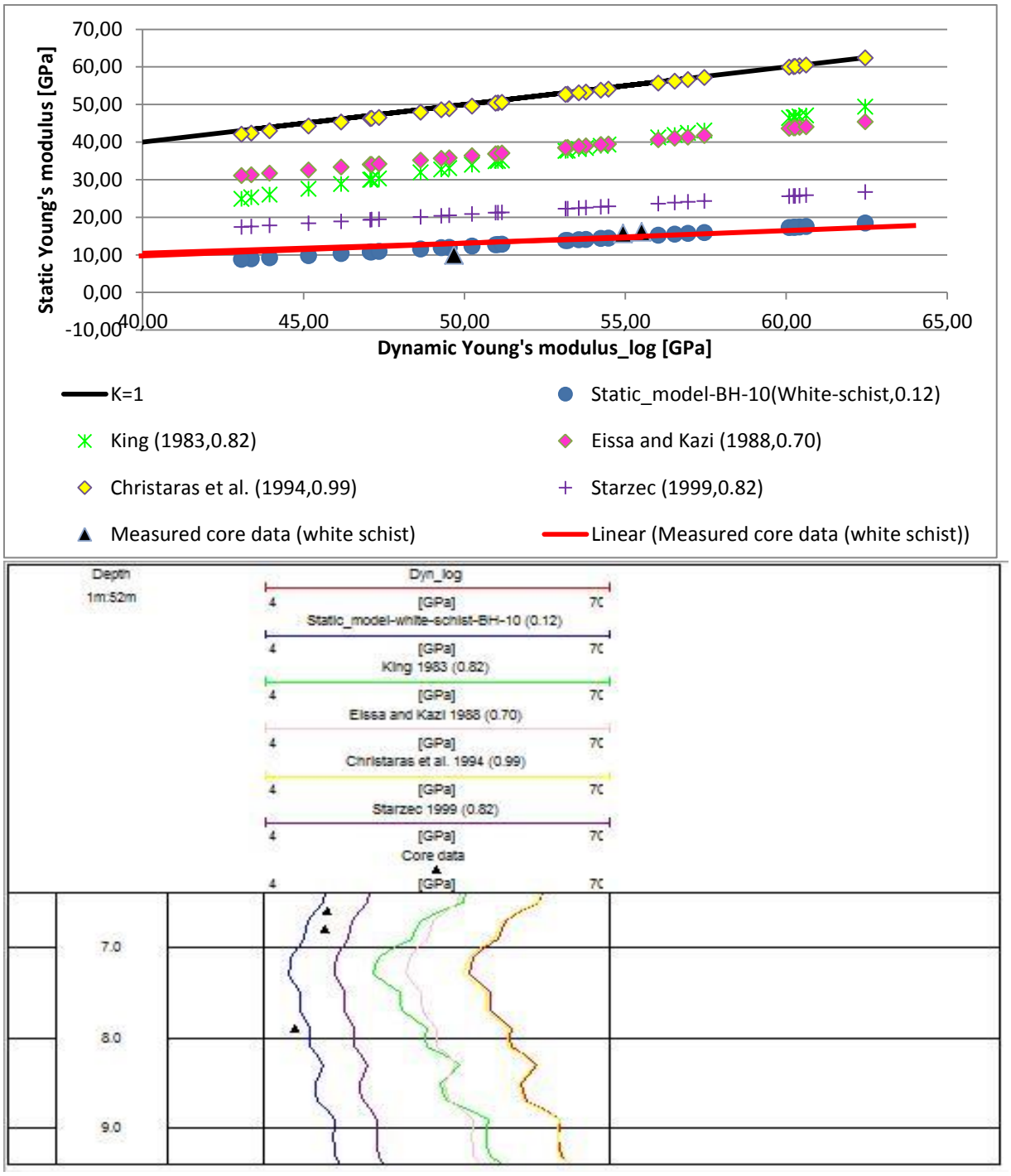

Figure 3.23: Comparison of current model with classic models for white schist using regression plot (top) and log section (bottom)

For the gneiss intervals in location 2, figure 3.24 show the corresponding regression plot as well as the log traces. The applicability of the model result obtained for the granite-gneiss rock interval (BH10) in location 1, was again tested in this location alongside the classic models and the model from the gneiss intervals. It could be seen that the Christaras' model maintained the prediction of high static values, and this time tend to overshoot the ideal k line. This of course, makes the model completely unacceptable for this location. Starzec's model which has low static values again, do however have the best fit with the measured core data. But it was not quite as good a match with the dynamic log data in the log traces section. The current model for the gneiss intervals in this location also show a poor match with the dynamic log data with minimal fit to the measured core data. It therefore, validates the poor model regression coefficient obtained for this rock interval earlier. Better matches could be observed for King's, Eissa and Kazi's and BH10 (location 1) models. And considering their closeness or fitness to the measured core data, BH10 model could be said to be the best out of these three.

Comparing the model result of the granite-amphibolite rock interval in this location with the classic models was more of a formality than quest for reliable deductions. This is because the measured core data and by extension the model result has been established to be highly erroneous. It is even more evident in the regression plot and log traces shown here in figure 3.25, than it was in earlier analysis. Two core data points could be seen above the ideal k line. This is totally wrong and goes against known principles in rock mechanics. The implication is that the red line of best fit in the regression plot must have been forced upwards sake of these two outlying data points. It would be safe to assume it is biased at this point. And models (Eissa and Kazi's and current model) that seemed to fit the measured core data in the plot might actually not fit. This can be seen clearer in the log traces. So, despite the model trace appearing to match the dynamic log trace, the model is actually not good given its lact of adequate fitness to the measured core data. Again, this is in total accord with the failure of the model correlation for this rock type as discussed in previous sections. Also, note that this time, the King's model just like the Christaras' model predicts high static values, even beyond the ideal k line (see dynamic values higher than 110 GPa). Starzec's model on the other hand predicts values much lower than the measured static data.

These observations however, do not in any way represent the true situation for the compared models, considering the obvious error in the measured data.

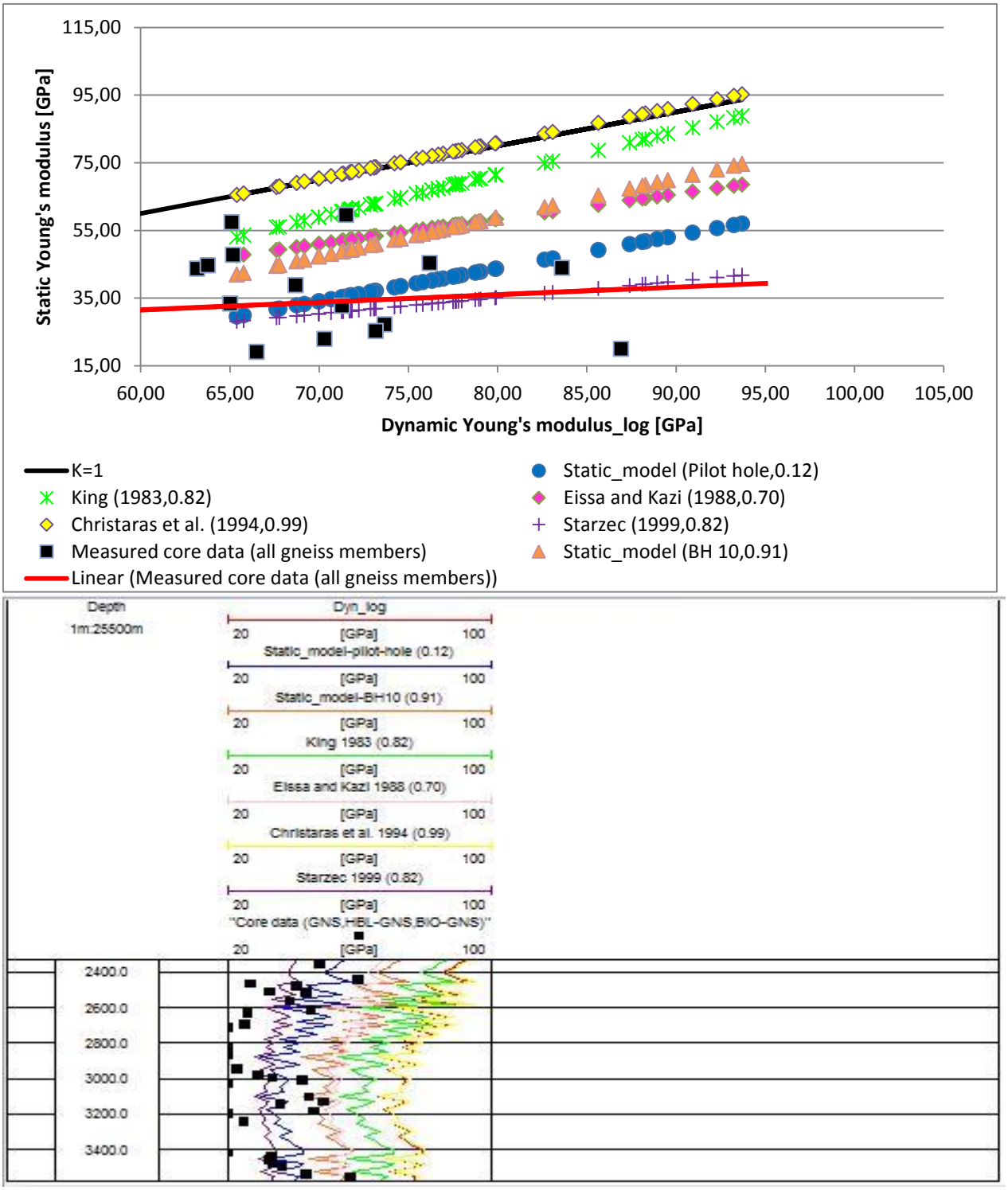

Figure 3.24: Comparison of current model with classic models for the combined gneiss intervals in the pilot borehole using regression plot (top) and log section (bottom)

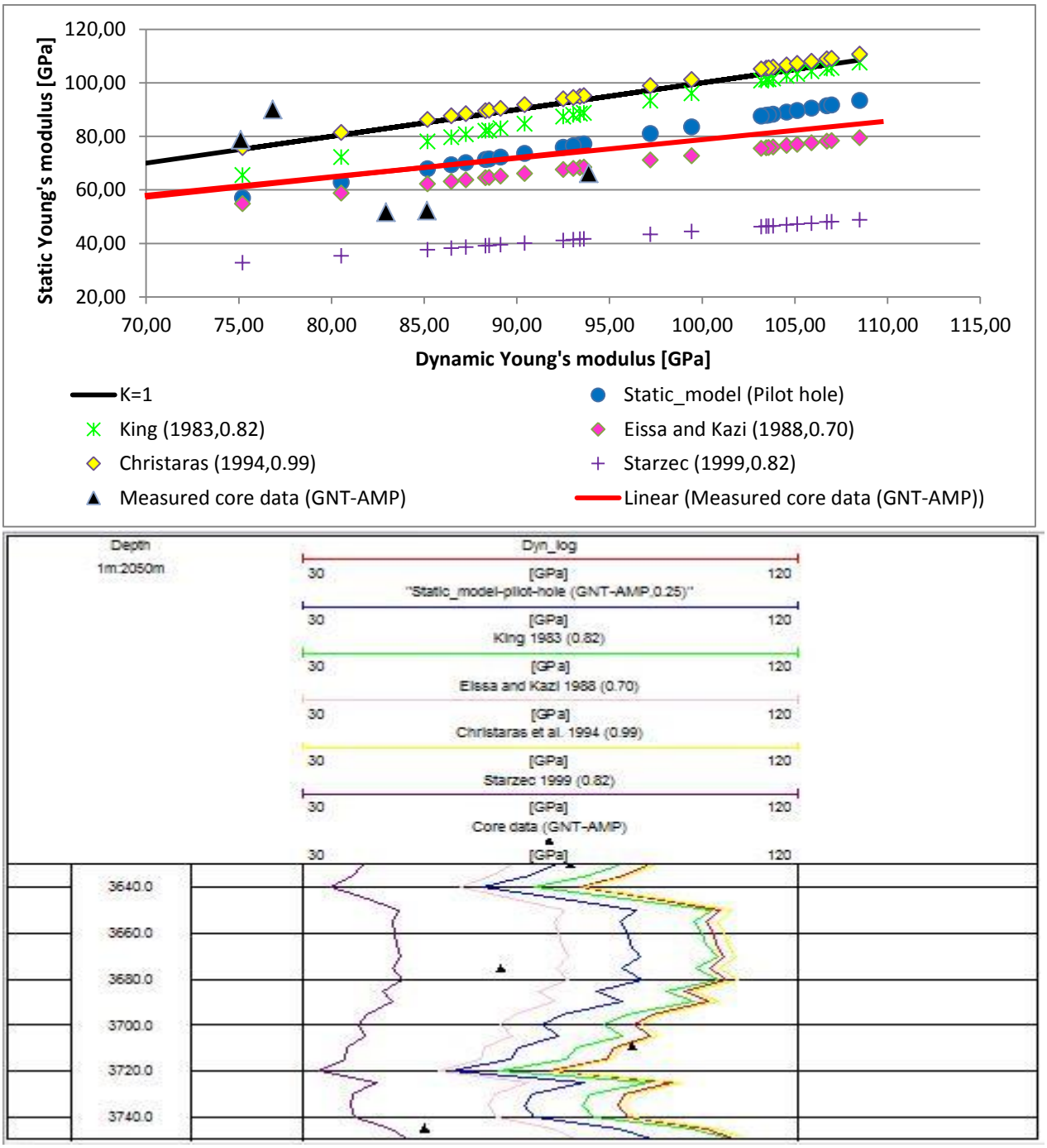

Figure 3.25: Comparison of current model with classic models for granite-amphibolite using regression plot (top) and log section (bottom)

4: Interpretations

In all comparative analysis involving field and laboratory measurements, efforts are usually made towards ensuring that in-situ conditions are replicated in the laboratory measurements. The hope is that this would correct measurement errors due to differential conditions and guarantee rendering of unbiased result. However, it does not work as hoped most times because of some immeasurable conditions like stress relief or mineral anisotropy. When the later is the case, there would be correlation errors as observed in the correlation of log and laboratory dynamic properties for the white schist interval at borehole 10 (location 1). The error subsequently compromised the model correlation of the static moduli of that rock interval with its dynamic moduli. At first, the error in that correlation result was suspected to be an interplay of factors creating significant difference in the in-situ rock properties and that of the cored sample measured in the laboratory. The factors as previously discussed include; presence of fractures, anisotropy, differential frequency of wave propagation and differential stress conditions. However, later application of the simplified defect model correction failed to improve the result for the white schist interval, and therefore suggests that the presence of cracks and possible foliations had very little or no influence on its poor results. The same could be said for the granite-amphibolite at location 2. Errors in their data as highlighted in section 3.1 might also have played significant role.

Correlation of the gneiss of different mineralogical compositions in location 2 was presumed a more holistic approach given the volume of data considered, and the depth interval covered. However, the extremely poor correlation result (standard) obtained for the combined unit begs for explanations. On one hand, it could be attributed to the differential diagenetic (possibly cement) properties of the associated minerals in the individual gneiss units, rather than mere compaction effect. On the other hand, it could be due to the reported poor data quality. Two observations tend to confirm the former as being the case. First, the deeper-placed granite-amphibolite from the same pilot borehole which was affected by the same or even worse data quality, produced a relatively better correlation result.

Secondly, it was established in section 3.3.2 that the solid matrix factor calculated for the combined gneiss unit (0.0067) is close to that calculated for the granite-gneiss unit from location 1 (0.0065). And that this calculated factor suggested consistent skeleton property for the gneiss rock type in the two different locations. Therefore, observed differences in moduli and other mechanical properties could reasonably be attributed to differential pore characteristics defined by cements and possibly micro grains of mostly the associated minerals of the gneiss intervals. Furthermore, if there occured an invasion of drilling muds into the walls of the boreholes (and into the pores) and unintentional inclusion of cores from such sections, that would also be enough to produce significant low correlation or outright non-correlation of the measured properties.

The application of model correlation equation to log data, in addition to giving estimates for the in-situ static properties, also helped in validation of the established model correlation result. This means that good model correlation results expectedly produced good static estimates that matched the dynamic log data reasonably well. However, some low correlation result (low regression coefficient) did produce log traces of static estimates that matched the dynamic log data. Therefore, the success and applicability of a model evidently depends more on its fitness to the measured core data and to a lesser extent the matching of its log trace to the dynamic log trace. It could therefore be tricky relying on only log traces for assessment of model efficiency or effectiveness. There was reasonable consistency in the model results of the rock intervals investigated when they were applied to their corresponding log data, except for the granite-amphibolite rock type. Its core data were proven very bad and should account for its unusually bad and contradictory results especially as recorded in the log sections.

In the comparisons with published works, it was observed that when the classic model equations were applied to the dynamic log data, they tend to produce results that are somewhat indicative of the original rock type(s) and location upon which the investigations of the respective authors were based. Christaras' model consistently suggested very high values for the in-situ static Young's moduli. In his published report, it was noted that most of the rocks he investigated were igneous and that they lack any physico-mechanical anisotropy whatsoever.

This means that the rocks besides being a lot different in composition, were in more perfect defectless condition than those used in current investigation. And as such should produce relatively higher in-situ static estimates that would tend towards converging to corresponding dynamic values. However, this does not provide justification for equality or overshoot of the static estimates to the dynamic log values as observed. Moreso, given that the available OBI data actually showed the existence of fractures and possible microcracks. And the defect model further confirmed same (irrespective of the level of correlation achieved). Starzec's model on the other hand, gave low static estimates close to the core static values. His model is suggestive of significant differences between the dynamic and static moduli. This is common with greatly defected (fractured) or poorly consolidated rock units. Its static estimates as predicted in current work are too low and showed poor correlation with the dynamic log values. King's model gave good and acceptable static estimates for all the rock types in this work. It was particularly the best for the white schist interval at location 1, where even the defect model failed. This might have to do with the fact that the majority rock type investigated in his igneous and metamorphic sample collection was biotite-schist. Eissa and Kazi's model just like King's model, also gave satisfactory static estimates. Their model estimates in current work tend to agree a lot with King's values in most rock types investigated. The defect model proved to be very efficient for granite-gneiss at location 1 and then for the composite gneiss intervals in location 2. This further strengthened the deduction that models work best when rocks of similar composition are considered.

5: Conclusion

The objective of most geomechanical rock elasticity investigations is to determine in-situ static properties that best agree or rather correlate with the easily measurable dynamic properties. The reality however remains that there is always a discrepancy in values of these measured properties whether they correlate or not. If repeated scientific measurements could be prone to disparity in measured values; then one would expect no less for these properties which are determined via entirely different methods and by unrelated apparatus. Therefore analysts sought more for correlations of the properties in terms of objective relationship equations rather than convergence of their corresponding values. Convergence of the values becomes a bonus when they occur. This however requires caution during interpretation as the convergence do not always entail good outcome. A good example is the result obtained by applying Christaras' model in current work. The model consistently produced convergent or approximately equal values for the estimated properties, even where there was poor correlation and/or model failure. Nevertheless, advances in rock mechanical analysis has made it possible to compute models that simultaneously correct measurement inadequacies, converge the values of the properties as much as possible, while maintaining high level correlation of the properties where such exist.

From the results of current work, one could see that violation of some established principles in the form of erroneous data yields bad correlation results. For instance, the record of higher velocities from the sonic log and subsequent computation of higher in-situ (log) dynamic Young's moduli compared to the corresponding laboratory dynamic Young's moduli at location 2, goes against the research findings of Fjaer et al. (2008) and most other published works. The result was poor correlations and failure of the defect model. Also consider the highlighted static data (two data points) for the granite-amphibolite at location 2 which were higher than their dynamic equivalents. These unusual data records might have contributed to the bad results obtained for that location. The errors would have been very likely, avoided if the composite uniaxial compressive test technique was adopted for the location.

At the very least, the records from both measurement approach would have been simultaneously documented, and there would not have been any case of mismatched data. Lastly, though some authors claim global applicability of their model correlation results and also suitability for all rock types; it was clear from the results in this investigation that such claims are usually exerggerated. One important finding here is that correlations of the properties of interest are best if models are applied to log data of the same or similar rock types. The good model static equation obtained for granite-gneiss at location 1 (in Austria) proved equally good for the combined gneiss intervals at location 2 (in Germany). Also, the observed efficiency of King's model for the white schist interval at location 1, interpreted as having to do with his use of majorly biotite-schist in his investigation, supports this finding. However, of more importance is the peculiarity of results to sample locations. It could be observed that while King's model as well as Eissa and Kazi's model were good for most of the rock types investigated here, current model obtained for granite-gneiss at location 1 proved much better at that location and even at location 2. So, while application of model equations at locations or regions other than the origins may give good results that saves time and resources; it does not always give the best possible estimates for in-situ static properties. Whenever such are desired, the recommendation is to derive model(s) based on data taken from the location of interest. And only consider good classic models when and where the current model fails.

Appendix

TM KB 10/13 3.40m						
Versuch durchgeführt am :			18-06-15			
Lithologie:			Granitgneis			
					Programmauswertung	
Force	**Uniaxial Stess**	**Height**	**Time**	**Strain**	**v_p**	**v_s**
[kN]	**[Mpa]**	**[mm]**	**[µs]**		**[m/s]**	**[m/s]**
10	1.22	196.27	79.94		-	-
50	6.09	196.18	66.58	0.00046	3542.4	-
100	12.17	196.09	60.78	0.00092	3936.0	2504.0
150	18.25	196.03	57.20	0.00122	4256.0	2588.2
200	24.34	195.98	55.39	0.00148	4435.9	2690.6
350	42.58	195.86	52.32	0.00209	4747.0	-
500	60.84	195.76	50.94	0.00260	4938.4	2950.0
350	42.57	195.83	51.99	0.00224	4821.0	2906.0
200	24.33	195.93	54.26	0.00173	4573.5	2752.6
150	18.25	195.97	55.54	0.00153	4374.3	2661.2
100	12.16	196.02	59.20	0.00127	4202.8	2537.1
50	6.07	196.09	63.67	0.00092	3802.4	-
10	1.22	196.19	73.68	0.00041	-	-

Table A.1: Measured stress and strain values for sample core at 3.40m depth (BH 10)

TM KB 10/13 3.60m						
Versuch durchgeführt am :			11-06-15			
Lithologie:			Granitgneis			
					Programmauswertung	
Force [kN]	**Uniaxial Stress [Mpa]**	**Height [mm]**	**Time [µs]**	**Strain**	**v_p [m/s]**	**v_s [m/s]**
12	1.47	191.69	81.96		-	-
50	6.11	191.62	68.04	0.00037	3378.3	2055.0
100	12.20	191.54	-	0.00078	-	-
150	18.29	191.48	56.52	0.00110	4152.7	2515.8
200	24.38	191.43	55.02	0.00136	4342.8	2642
500	60.95	191.23	49.62	0.00240	4969.6	2951.1
200	24.37	191.39	53.28	0.00157	4507.5	-
150	18.29	191.43	55.34	0.00136	4356.6	2603
100	12.19	191.48	57.68	0.00110	4109.0	2499.7
50	6.09	191.55	63.08	0.00073	3683.7	-
10	1.22	191.63	77.08	0.00031	-	-

Table A.2: Measured stress and strain values for sample core at 3.60m depth (BH 10)

TM KB 10/13 3.80m						
Versuch durchgeführt am :			11-06-15			
Lithologie:			Granite-gneiss			
					Programmauswertung	
Force [kN]	**Uniaxial Stress [Mpa]**	**Height [mm]**	**Time [µs]**	**Strain**	**v_p [m/s]**	**v_s [m/s]**
12	1.47	197.18	83.82		-	-
50	6.12	197.09	66.81	0.00046	3457.7	2004.8
100	12.22	197.01	61.65	0.00086	3895.0	2266.8
150	18.33	196.95	59.07	0.00117	4116.0	2528
200	24.43	196.90	57.02	0.00142	4309.5	2621.1
500	61.07	196.69	51.33	0.00249	4878.2	2972
200	24.42	196.86	55.32	0.00162	4448.8	2692.7
150	18.30	196.90	57.06	0.00142	4284.2	2592.2
100	12.21	196.95	59.31	0.00117	4082.7	-
50	6.10	197.02	64.08	0.00081	3739.9	2299.0
10	1.22	197.11	71.82	0.00036	-	-
2	0.24	197.13	-	0.00025	-	-

Table A.3: Measured stress and strain values for sample core at 3.80m depth (BH 10)

TM KB 10/13 6.60m						
Versuch durchgeführt am :			18-06-15			
Lithologie:			White Schist			
					Programmauswertung	
Force [kN]	**Uniaxial Stress [Mpa]**	**Height [mm]**	**Time [µs]**	**Strain**	**v_p [m/s]**	**v_s [m/s]**
10	1.23	188.24	-		-	-
50	6.14	187.35	99.05	0.00473	-	-
100	12.22	187.02	69.62	0.00648	3148.5	-
150	18.33	186.87	61.89	0.00728	3741.1	2170
200	24.43	186.77	57.39	0.00781	4087.8	2359
350	42.75	186.58	52.14	0.00882	4600.1	2739
500	61.07	186.45	50.37	0.00951	4844.1	2902.8
350	42.74	186.52	50.06	0.00914	4692.3	2827.3
200	24.42	186.64	54.42	0.00850	4356.7	2559.2
150	18.32	186.70	55.91	0.00818	4146.1	-
100	12.21	186.78	60.17	0.00776	3803.3	2189.9
50	6.11	186.92	70.91	0.00701	3017.3	-
10	1.23	187.30	-	0.00499	-	-

Table A.4: Measured stress and strain values for sample core at 6.60m depth (BH 10)

TM KB 10/13 6.80m						
Versuch durchgeführt am :			18-06-15			
Lithologie:			White Schist			
					Programmauswertung	
Force	**Uniaxial Stress**	**Height**	**Time**	**Strain**	**v_p**	**v_s**
[kN]	**[Mpa]**	**[mm]**	**[µs]**		**[m/s]**	**[m/s]**
10	1.24	188.87	-	-	-	-
50	6.14	187.96	105.00	0.00484	2004.3	1200.9
100	12.20	187.61	71.94	0.00669	3035.8	-
150	18.29	187.43	63.99	0.00760	3535.7	2045.1
200	24.38	187.32	60.15	0.00822	3854.3	2253.1
350	42.67	187.11	53.45	0.00933	4461.4	2823
500	60.95	186.97	50.84	0.01007	4789.2	2897.9
350	42.67	187.04	52.26	0.00969	4566.4	-
200	24.37	187.17	56.24	0.00902	4163.0	2532.7
150	18.29	187.23	59.53	0.00867	3912.9	2403
100	12.19	187.32	63.97	0.00819	3549.1	2126.2
50	6.09	187.49	75.76	0.00732	-	-
10	1.20	187.89	-	0.00517	-	-

Table A.5: Measured stress and strain values for sample core at 6.80m depth (BH 10)

TM KB 10/13 7.90m						
Versuch durchgeführt am :			11-06-15			
Lithologie:			White Schist			
					Programmauswertung	
Force	**Uniaxial Stress**	**Height**	**Time**	**Strain**	**v_p**	**v_s**
[kN]	**[Mpa]**	**[mm]**	**[µs]**		**[m/s]**	**[m/s]**
12	1.46	195.47	183.90		-	-
50	6.14	194.53	119.80	0.00482	1761.2	1040
100	12.20	193.98	94.00	0.00765	-	-
150	18.30	193.71	70.41	0.00903	3349.1	-
200	24.40	193.52	64.65	0.00996	3677.7	2231.3
500	60.95	192.90	56.60	0.01318	4488.1	2783
200	24.37	193.19	63.17	0.01168	3917.1	2383.3
150	18.28	193.29	65.93	0.01119	3713.5	2259
100	12.19	193.43	73.67	0.01047	3235.2	-
50	6.09	193.68	91.62	0.00915	2474.5	1456
10	1.19	194.34	158.60	0.00581	-	-

Table A.6: Measured stress and strain values for sample core at 7.90m depth (BH 10)

TM KB 09/13 15.40m						
Versuch durchgeführt am :			11-06-15			
Lithologie:			Granitgneis			
					Programmauswertung	
Force	**Uniaxial Stress**	**Height**	**Time**	**Strain**	v_p	v_s
[kN]	**[Mpa]**	**[mm]**	**[µs]**		**[m/s]**	**[m/s]**
12	1.47	197.59	70.94		-	-
50	6.11	197.55	64.43	0.00020	3933.7	2362
100	12.22	197.49	60.44	0.00051	4222.6	2569.0
150	18.32	197.44	58.94	0.00076	4434.9	2641.0
200	24.43	197.39	56.42	0.00101	4598.0	2722.2
500	61.09	197.16	53.55	0.00218	5150.5	-
200	24.43	197.32	53.40	0.00137	4714.9	2868.4
150	18.32	197.36	54.66	0.00116	4581.2	2714.0
100	12.21	197.41	56.60	0.00091	4413.4	2685
50	6.11	197.47	59.93	0.00061	4093.5	2491
10	1.22	197.53	67.16	0.00030	3519.2	-
2	0.24	197.55	-	0.00020	-	-

Table A.7: Measured stress and strain values for sample core at 15.40m depth (BH 9)

TM KB 09/13 15.80m						
Versuch durchgeführt am :						
Lithologie:			Granitgneis			
					Programmauswertung	
Force	**Uniaxial Stress**	**Height**	**Time**	**Strain**	v_p	v_s
[kN]	**[Mpa]**	**[mm]**	**[µs]**		**[m/s]**	**[m/s]**
1.5	0.18	196.65	77.32		-	-
4	0.49	196.65	-	0.00000	-	-
50	6.11	196.59	64.60	0.00031	3643.2	1975.3
100	12.21	196.52	60.87	0.00066	4006.6	-
150	18.33	196.47	57.38	0.00092	4252.7	2339.8
200	24.43	196.43	55.78	0.00112	4460.3	-
500	61.07	196.23	48.69	0.00214	5118.1	2754.0
200	24.43	196.38	52.95	0.00137	4622.9	2452.6
150	18.32	196.42	56.02	0.00117	4469.1	2387.8
100	12.21	196.46	57.57	0.00097	4219.5	2322.2
50	6.11	196.52	65.70	0.00066	3596.6	1949.6
2	0.24	196.61	84.80	0.00020	-	-

Table A.8: Measured stress and strain values for sample core at 15.80m depth (BH 9)

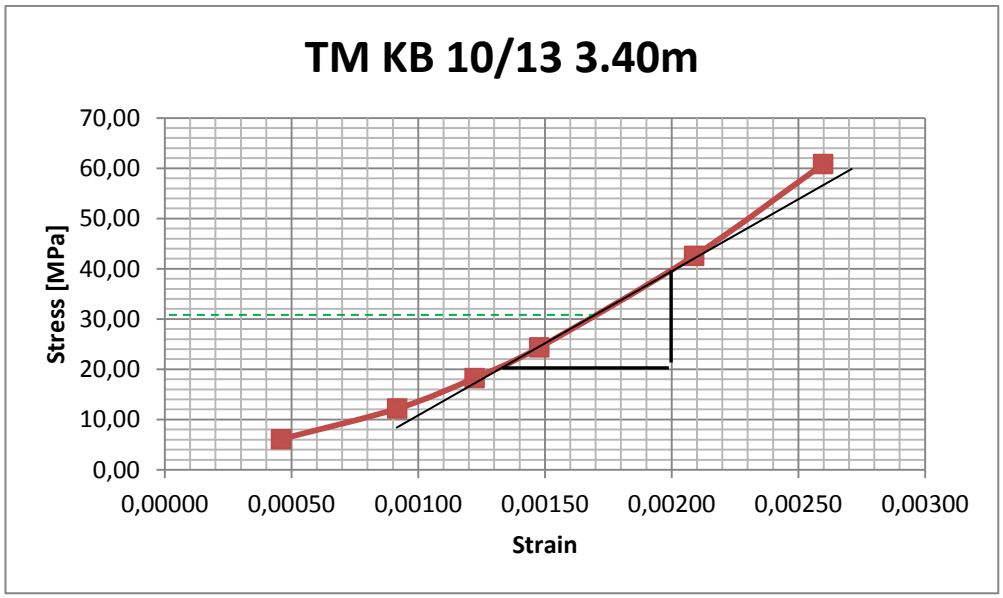

Figure A.1: Stress-strain plot showing only the loading session (3.40m depth, BH 10)

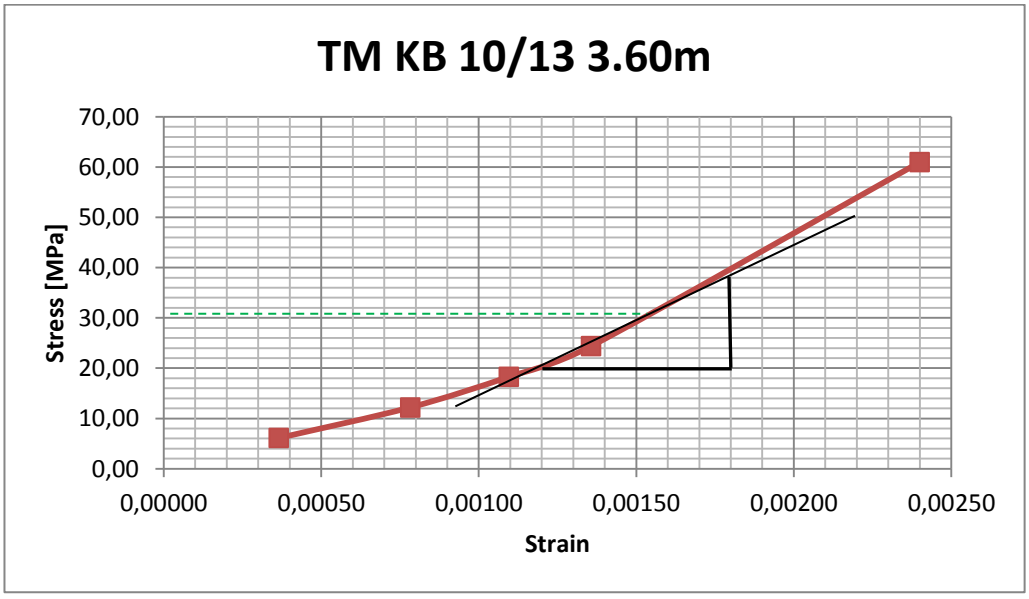

Figure A.2: Stress-strain plot showing only the loading session (3.60m depth, BH 10)

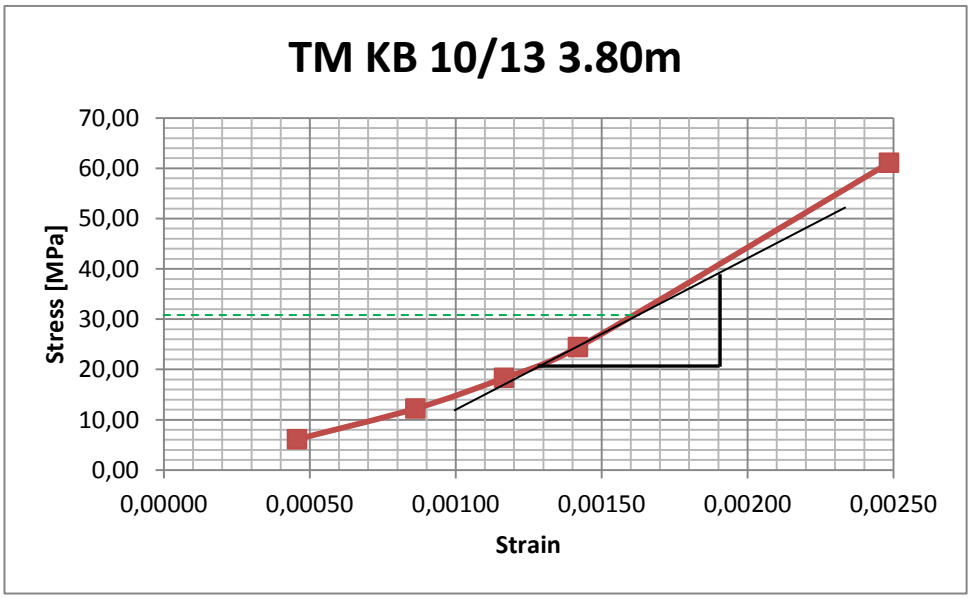

Figure A.3: Stress-strain plot showing only the loading session (3.80m depth, BH 10)

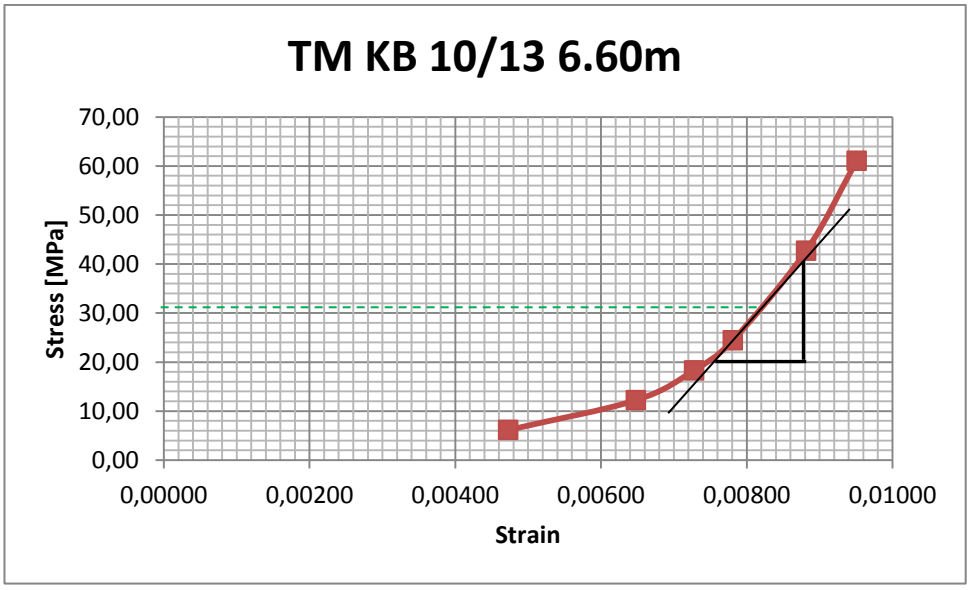

Figure A.4: Stress-strain plot showing only the loading session (6.60m depth, BH 10)

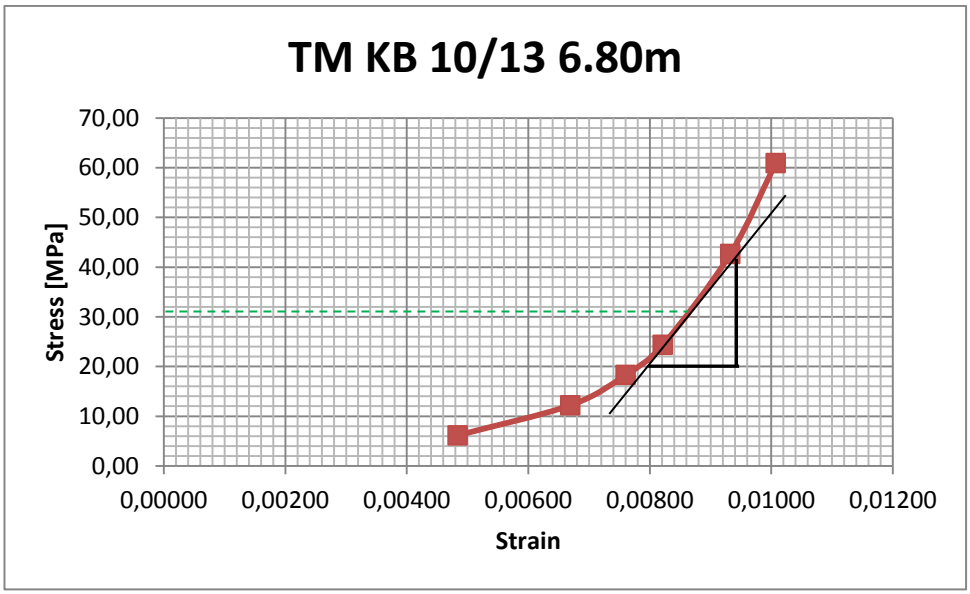

Figure A.5: Stress-strain plot showing only the loading session (6.80m depth, BH 10)

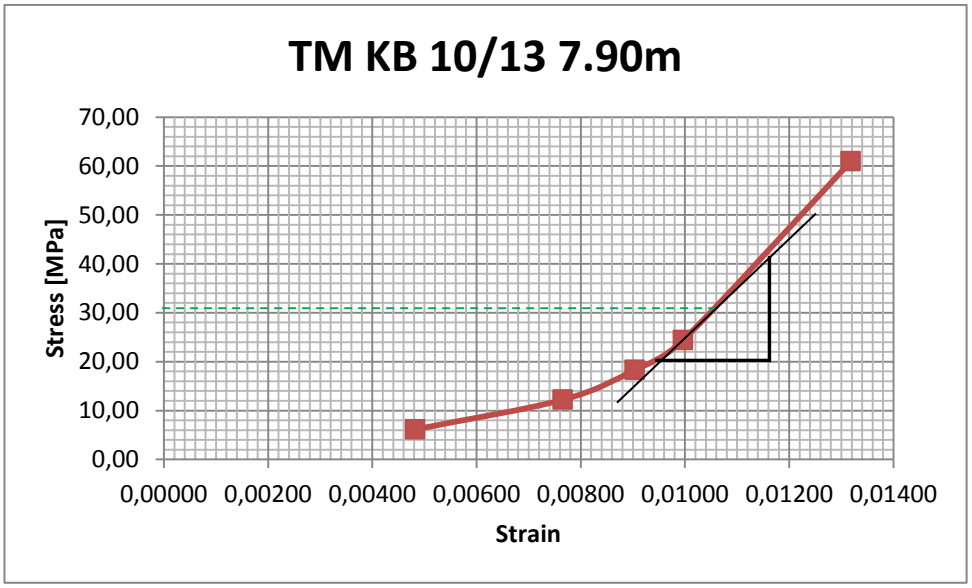

Figure A.6: Stress-strain plot showing only the loading session (7.90m depth, BH 10)

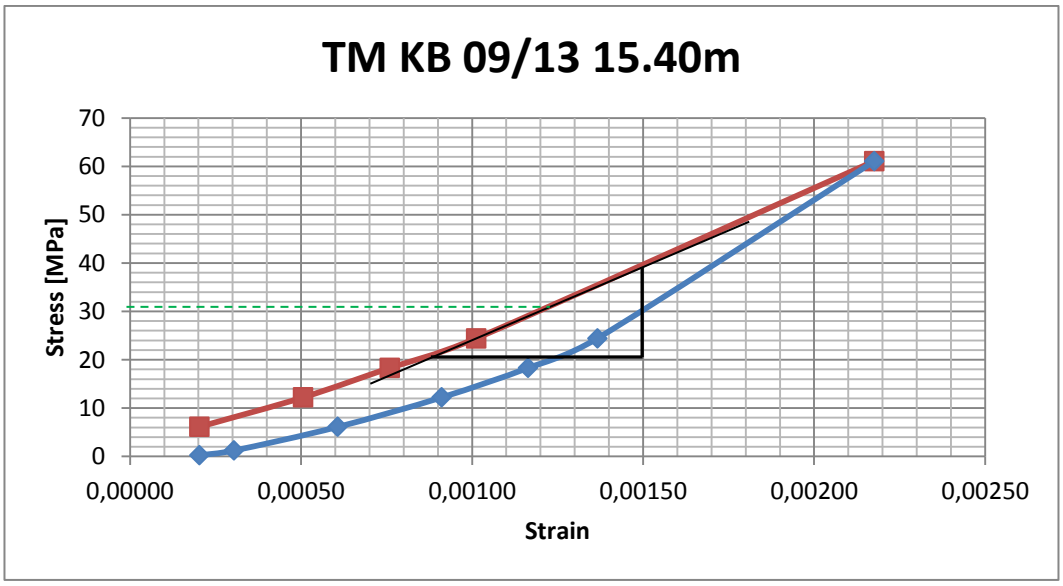

Figure A.7: Stress-strain plot showing loading and unloading sessions (15.40m depth, BH 9)

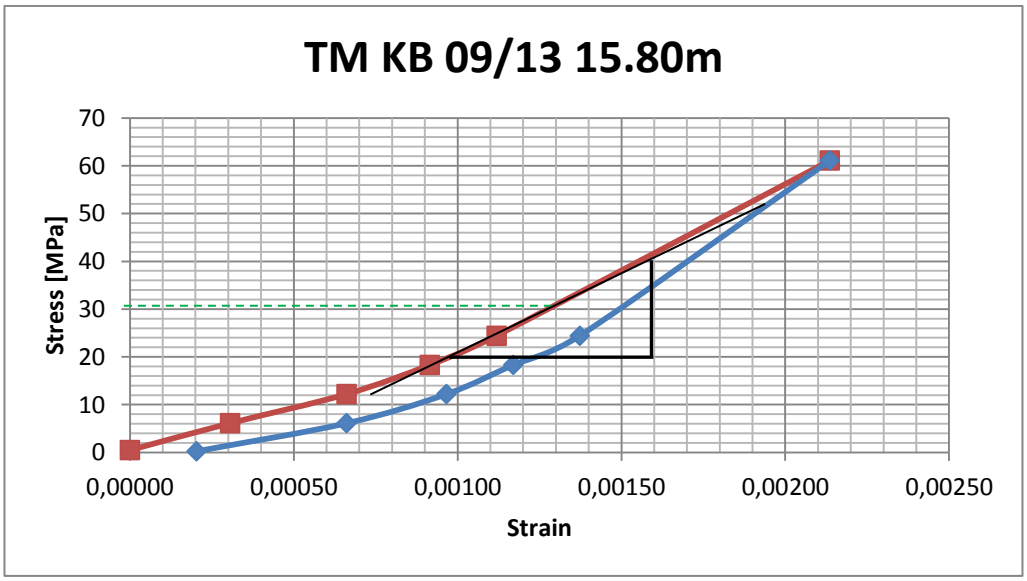

Figure A.8: Stress-strain plot showing loading and unloading sessions (15.80m depth, BH 9)

REFERENCES

Brotons, V., Tomas, R., Ivorra, S., Grediaga, A., Martinez-Martinez, J., Benavente, D., and Gomez-Heras, M., 2016. Improved correlation between the static and dynamic elastic modulus of different types of rocks. *Materials and Structures*, **49**(8):3021-3037.

Budiansky, B., and O'Connell, R.J., 1976. Elastic moduli of a cracked solid. *Int. J. Solids Structures.*, vol**.12**, pp. 81-97.

Burns, D.R., Cheng, C.H., Schmitt, D.P., and Toksoz, M.N., 1988. Permeability estimation of full waveform acoustic logging data. *The Log Analyst*, vol**.29**, pp. 112-122.

Castagna, J.P., Batzle, M.L., and Eastwood, R.L., 1985. Relationships between compressional-wave and shear-wave velocities in clastic silicate rocks. *Geophysics*, **50**:571-581

Christaras, B., Auger, F., and Mosse, E., 1994. Determination of the moduli of elasticity of rocks. Comparison of the ultrasonic velocity and mechanical resonance frequency methods with direct static methods. *Materials and Structures*, **27**:222-228.

Christensen, D.M., 1964. A theoretical analysis of wave propagation in fluid filled drill holes for the interpretation of the 3-Dimensional velocity log. *Transactions of the 5th annual logging symposium of the Society of Professional Well Log Analysts, Midland, Texas*.

Christensen, D.M,, 1966. The determination of the in-situ elastic properties of rock salt with a 3-Dimensional velocity log. *Proceedings of the Northern Ohio Geological society, Cleveland, Ohio*, 104-115.

Eissa, E.A., and Kazi, A., 1988. Relation between static and dynamic Young's moduli of rocks. *Int. J. Rock Mech. Mining Sci. & Geomech. Abstracts*, vol.**25,** No.6, pp. 479-482.

Elkatatny, S., Mahmoud, M., Mohamed, I., and Abdulraheem, A., 2017. Development of a new correlation to determine the static Young's modulus. *J. Petrol. Explor. Prod. Technol,* DOI 10.1007/S13202-017-0316-4.

Entwisle, D.C., and McCann, D.M., 1990. An assessment of the use of Christensen's equation for the prediction of shear wave velocity and engineering parameters. In: Hurst, A., Lovell, M.A., and Morton, A.C., (eds). Geological applications of wireline logs. *Geological Society London, special publication,* **48**:347-354.

Fjaer, E., Holt, R.M., Raaen, A.M., Risnes, R., and Horsrud, P., 2008. Petroleum related rock mechanics, second edition. *Elsevier Science publication*, *volume* **53**, pp. 175-218, 251-284.

Gegenhuber, N., and Steiner-Luckabauer, C., 2012. Vp/Vs automatic picking of ultrasonic measurements and their correlation of petrographic coded carbonates from Austria. *74th EAGE conference and exhibition, Copahagen*.

Gegenhuber, N., Schifko, T., and Pittino, G., 2017. Petrographic coded model concept for the correlation between geomechanical and elastic properties and its application on log data for Alpine rocks. *Austrian Journal of Earth Sciences*, *volume* **110/1**, DOI:10.17738/ajes.2017.0007.

Hongkui, G., Yingsong, L., and Lili, S., 2001. Difference of rock elastic parameters under static and dynamic loading. Frontiers of Rock Mechanics and sustainable development in the 21st century, pp. 69-71.

Kassam, A., Milkereit, B., Gerrie, V., and Drielsma, C., 2016. Linking seismic and geotechnical parameters using velocity-density relationship. In: Optimizing Resources, *Geoconvention March 2016, Calgary-Canada*.

King, M.S., 1983. Static and dynamic elastic properties of rocks from the Canadian Shield. *Int. J. Rock Mech. Mining Sci. & Geomech. Abstracts*, vol.**20,** No.5, pp. 237-241.

McCann, D.M., and Entwisle, D.C., 1992. Determination of Young's modulus of the rock mass from geophysical well logs. In: Hurst, A., Griffiths, C.M., and Worthington, P.F.,(eds). Geological applications of wireline log II. *Geological Society London, special publication*, **65**:317-325.

Mockovciakova, A., and Pandula, B., 2003. Study of the relation between the static and dynamic Young's moduli of rocks. *Metalurgija*, **42**(1):37-39.

Pittino, G., Gegenhuber, N., Reiter, F., and Fröhlich, R., 2016. Ultrasonic wave measurements during uniaxial compression tests. Proceedings of the 2016 ISRM international symposium, EUROCK 2016. *Rock mechanics and Rock Engineering : From the past to the future*. *Taylor and Francis Ltd*, s.365-369.

Prensky, S.E., 1999. Advances in borehole imaging technology and applications. In: Lovell, M.A., Williamson, G., and Harvey, P.K., (eds). Borehole Imaging: applications and case histories. *Geological Society London, special publications*, **159**:1-43.

Schön, J.H., 2015. Physical properties of rocks: Fundamentals and Principles of Petrophysics, second edition. *Development in Petroleum Science series*, vol.**65**, pp. 167-243, 269-293.

Starzec, P., 1999. Characterization of the physical properties of rocks. Thesis, department of Geology, *Chalmers University of technology, Sweden*. Publ. A90.

Stevens, J.L., and Day, S.M., 1986. Shear velocity logging in slow formations using the stoneley wave. *Geophysics*, vol.**51**, pp. 137-147, DOI:10.1190/1.1442027.

Williams, D.M., Zemanek, J., Angona, F.A., Dennis, C.L., and Caldwell, R.L., 1984. The long space acoustic logging tool. *Transactions of the Society of Professional Well Log Analysts, 25th annual logging symposium*, paper T.

Williams, J.H., and Johnson, C.D., 2004. Acoustic and optical borehole-wall imaging for fractured-rock aquifer studies. *Journal of applied Geophysics*, vol.**55**, Issue 1-2, pp.151-159.

Zemanek, J., Glenn, E.E., Norton, L.J., and Caldwell, R.L., 1970. Formation evaluation by inspection with the borehole televiewer. *Geophysics*, vol.**35**, No.2, pp. 254-269.

Zisman, W.A., 1933, Comparison of statically and seismologically determined elastic constants of rocks. *Proc. Natl. Acad. Sci., U.S.*, **19**:680-686.